Redoubled Effect of a Neutron Spin Rotation in Deformed Noncentrosymmetric Crystal for the Bragg Diffraction Scheme[¶]

V. V. Fedorov, I. A. Kuznetsov, E. G. Lapin, S. Yu. Semenikhin, and V. V. Voronin*

St. Petersburg Institute of Nuclear Physics, Russian Academy of Sciences, Gatchina, 188300 Russia
*e-mail: vvv@mail.pnpi.spb.ru
Received September 9, 2004; in final form, October 12, 2004

A doubled effect of a neutron spin rotation in a noncentrosymmetric quartz crystal for the Bragg reflected neutrons from the deformed exit crystal side is first observed. The effect arises due to a neutron Schwinger interaction with the crystal and depends on the value of the crystal deformation near its back exit face. The electric field acting on a neutron in the quartz crystal is about $\sim 10^8$ V/cm. This field affects the neutron during the whole time of its passage through the crystal, both there and back. This time is limited only by the available size of the crystal (14 and 27 cm in our case) or the neutron absorption length. Observation of such effects gives a real perspective on the essential improvement of the scheme and sensitivity of the experiment in the search for a neutron electric dipole moment (EDM) by the crystal-diffraction technique. Moreover, the presented experimental scheme can be applied for a neutron with an energy close to the *P* wave resonance to search for the *T*-odd part of a neutron–nuclei interaction, for example, because of relatively low requirements of crystal quality. © 2004 MAIK "Nauka/Interperiodica".

PACS numbers: 14.20.Dh; 61.12.Gz

1. INTRODUCTION

Recently, a new method of the search for the neutron electric dipole moment (EDM) was proposed [1, 2] and developed [3, 4]. It is based on the interaction of the diffracted neutron with the interplanar electric field of a crystal without a center of symmetry. The value of the electric field can reach 10^8–10^9 V/cm. An estimated sensitivity of the method for the available noncentrosymmetric quartz crystal turned out to be $\sim 10^{-25}$ e cm per day [3, 4]. We note that the sensitivity of any method to measure the neutron EDM is determined by the product $E\tau\sqrt{N}$, where E is the value of the electric field, τ is the time of neutron interaction with the field, and N is the accumulated statistics. For the quartz crystal, the maximum value of the electric field is $\sim 2 \times 10^8$ V/cm [5, 6], and $\tau \approx 1$ ms [3, 7] is restricted by absorption in the crystal. The future essential progress of this method could be expected with using other crystals. Now, the most promising ones seem to be the BSO ($Bi_{12}SiO_{20}$, $Bi_4Si_3O_{12}$) and PbO crystals. Calculations have shown that the sensitivity of the method using the BSO or PbO crystals can be improved by about an order of magnitude in comparison with that using the quartz one. Unfortunately, the present scheme of the experiment [4] does not allow one to realize the potential of the BSO and PbO crystals, so additional investigations

of the neutron spin effects in a noncentrosymmetric crystal are needed to develop the new experimental scheme.

Originally, two different crystal-diffraction schemes for a neutron EDM search were proposed. The first was the Laue diffraction method [1–3], and the second was the Bragg diffraction one [8, 9]. The main advantage of the Laue diffraction scheme is the possibility of increasing the time τ that the neutron stays in the crystal using the Bragg angles θ_B close to $\pi/2$ [2]. This bonus allows us to reach a time of neutron stay in the quartz crystal that is close to the time of neutron absorption $\tau_a \approx 1$ ms [3, 7]. A detailed consideration of the Laue diffraction method has shown that we cannot essentially increase the sensitivity of the method using other noncentrosymmetric crystals with advanced parameters according to the following factors: we have to use the crystals with the thickness determined by [4]

$$L_0 = \frac{\pi m_p c^2}{2\mu_n e E_g},\qquad(1)$$

to get the depolarization effect (spin rotation angles equal to $\pm\pi/2$ for two kinds of neutron waves propagating in the crystal); here, E_g is the electric field affecting the neutron for the exact Bragg condition. Therefore, the greater value of the field E_g requires a decrease in the crystal thickness and, accordingly, the time of neu-

---

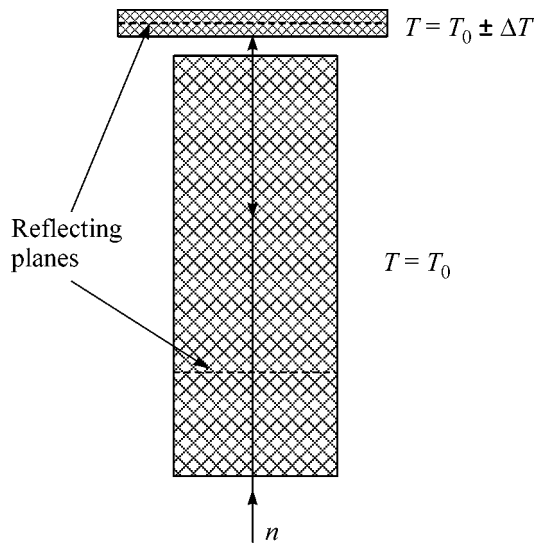[¶] This article was submitted by the authors in English.

Fig. 1. Two crystals in parallel position. Neutrons reflected by the small crystal pass twice through the large crystal. The deviation parameter Δ for the large crystal is determined by the temperature difference ΔT.

tron passage through the crystal; we cannot increase the sensitivity using the Bragg angles extremely close to $\pi/2$, because of the very low luminosity of the experiment for such angles [10].

The main advantage of the Bragg diffraction scheme [8, 11] in comparison with the Laue diffraction one [4] is that the effect of spin rotation arises due to Schwinger or EDM interaction with the interplanar electric field for the neutron passing through the crystal near the Bragg condition, and one can control the sign and value of the electric field acting on the registered neutrons by selecting the neutrons with the different sign and value of the parameter of deviation from the Bragg condition. Moreover, the sensitivity of the Bragg diffraction method is not limited by the given crystal thickness, as it is for the Laue diffraction one [4]. However, in this case, the effect due to neutron EDM does not increase for the Bragg angles close to $\pi/2$ as it does for the Laue diffraction scheme. For the Bragg diffraction, the time of neutron stay in the crystal, τ, is determined by the total neutron velocity v, while for the Laue diffraction, τ is determined by the component along the crystallographic plane, but this fault in principle can be repaired by increasing the crystal thickness. The main problem, which the authors [11] met and solved in a very complicated way, was how to obtain neutrons with the given deviation parameter.

Here also a very simple solution of this problem is given.

2. SPIN ROTATION FOR THE BRAGG–REFLECTED NEUTRONS

Let us consider the symmetric Bragg diffraction case. A neutron falls on the crystal in the direction close to the Bragg one for the crystallographic plane g. Deviation from the exact Bragg condition is described by the parameter $\Delta = E_k - E_{k_g}$, where $E_k = \hbar^2 k^2/2m$ and $E_{k_g} = \hbar^2|\mathbf{k} + \mathbf{g}|^2/2m$ are the energies of a neutron in the states $|k\rangle$ and $|k + g\rangle$, respectively.

In this case, the neutron wave function inside the crystal in the first order of perturbation theory can be written [12]

$$\psi(\mathbf{r}) = e^{-i\mathbf{k}\mathbf{r}} + a \cdot e^{-i(\mathbf{k} + \mathbf{g})\mathbf{r}}, \tag{2}$$

where

$$a = \frac{|V_g|}{E_k - E_{k_g}} = \frac{|V_g|}{\Delta}. \tag{3}$$

Here, V_g is the g-harmonic of the interaction potential of the neutron with the crystal. For simplicity, we consider the case $a \ll 1$, so we can use perturbation theory.

The electric field affecting the diffracted neutron will be equal to [12]

$$\mathbf{E} = \mathbf{E}_g \cdot a, \tag{4}$$

where $\mathbf{E}_g$ is the interplanar electric field for the exact Bragg condition.

One can see that the sign and value of electric field (4) are determined by the sign and value of the deviation Δ from the exact Bragg condition; therefore, to have the given electric field and thus the effect of neutron spin rotation, we should select from the whole beam the neutrons with the corresponding deviation parameter Δ.

The presence of the electric field will lead to an appearance of the Schwinger magnetic field

$$\mathbf{H}_S = 1/c[\mathbf{E} \times \mathbf{v}_\parallel]. \tag{5}$$

The neutron spin will rotate around $\mathbf{H}_S$ by the angle

$$\varphi_s = \frac{4\mu H_S L_c}{\hbar v_\perp}, \tag{6}$$

where L_c is the crystal thickness and $v_\parallel$ and $v_\perp$ are the components of neutron velocity parallel and perpendicular to the crystallographic plane, correspondingly.

In the experiment in [11], the effect of neutron spin rotation due to spin–orbit (Schwinger) interaction was experimentally observed in the Bragg diffraction scheme for small (~a few Bragg width) deviations from the Bragg condition, but the measured value was about three times less than was theoretically predicted. In the experiment in [13], we observed the effect of neutron spin rotation in neutron optics for large (~10^3–10^4 Bragg width) deviations from the exact Bragg condition. The measured effect coincided with the theoretical one.

The main idea of the present work is the following. We use a small controlled variation of the interplanar distance Δd (caused by heating, for example) near the exit crystal edge. Some part of the neutrons passed through the crystal will reflect from this small crystal part. These back-diffracted neutrons have the deviation parameter for the main part of the crystal determined by Δd, and thus they propagate under the corresponding electric field both there and back. Thermal deformation of the crystal edge is used to create such a variation of the interplanar distance.

We can use also two separate crystals in parallel positions for this purpose (see Fig. 1). One can heat (or cool) the second small crystal. The neutrons passed through the first crystal with the corresponding Bragg wavelength will be reflected by the second crystal with the given deviation parameter for the first (large) crystal. This deviation parameter will directly depend on the temperature difference between crystals.

The value of the wavelength Bragg width for the (110) quartz plane ($d = 2.45$ Å) is $\Delta\lambda_B/\lambda \approx 10^{-5}$. To shift the reflex wavelength by one Bragg width, we should have the same value of $\Delta d/d$. The linear coefficient of thermal expansion for a quartz crystal is $\Delta L/L \approx 10^{-5}$ per degree. Therefore, the deviation $\pm\Delta\lambda_B$ corresponds to a difference in the crystal temperatures of $\Delta T \approx \pm1°$. We note that the different signs of this temperature difference will correspond to different signs of the electric field acting on the neutron.

3. EXPERIMENT

A scheme of the neutron behavior in the crystal is shown in Fig. 2. Two samples of quartz crystal were used in this experiment with thicknesses along X axis of $L_c = 14$ and 27 cm. The Peltier element was attached to the back face of the crystal. That allows us to create the temperature gradient in the crystal along the neutron trajectory. So, the Bragg condition will vary along the neutron trajectory and different parts of crystal will reflect the neutrons with different λ. Therefore, the reflected beam will contain not only the reflex from the entrance crystal face (corresponding to Bragg condition for d) but also the reflection from the back exit face (corresponding to $d \pm \Delta d$) that twice pass through the crystal there and back. Moreover, the value of the deviation parameter Δ for this reflection directly depends on the value of the temperature gradient. In the case of higher temperature of the back crystal face, the neutron with $E_k - E_{k_g} > 0$ will be reflected, while in the case of its lower temperature, the neutron with $E_k - E_{k_g} < 0$ will be reflected.

Examples of the time of flight spectra of the reflected neutrons for the Bragg angle ~90° are shown in Fig. 3. One can see formation of the reflex from the back crystal surface and an increase in its intensity with the rise of the temperature gradient.
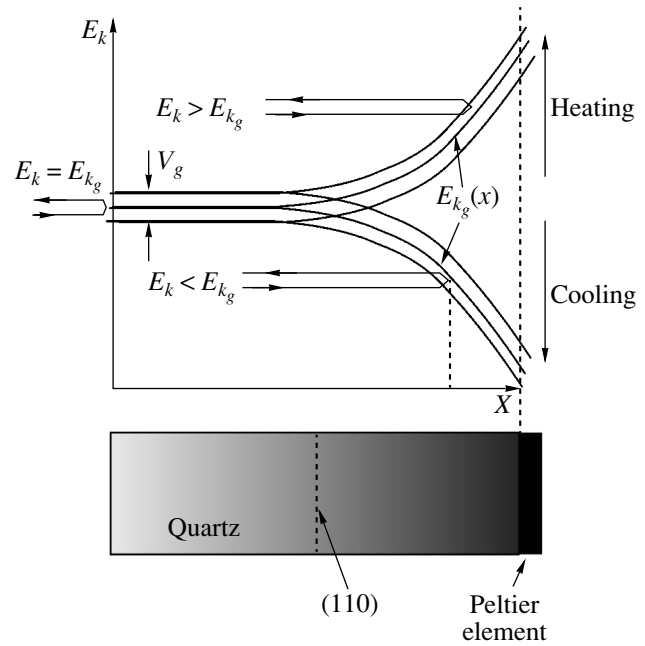

Fig. 2. Passage of the neutron through the crystal. Presence of the interplanar distance gradient results in the formation of the reflex near the back face of crystal.
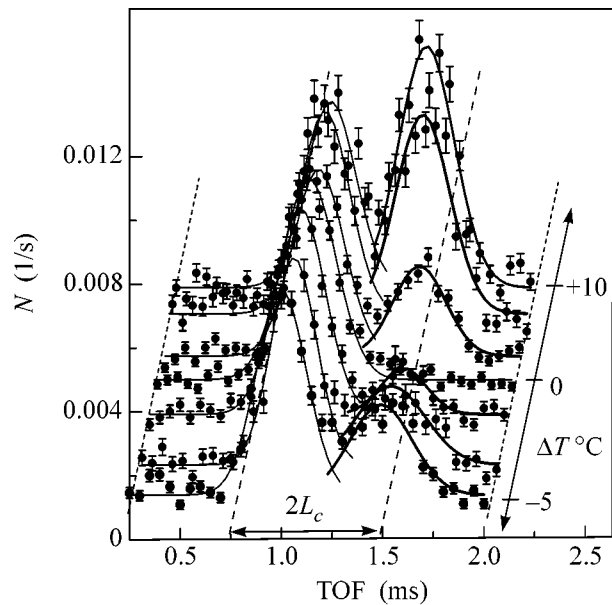

Fig. 3. Dependence of the time of flight (TOF) spectra of the neutron reflected by the (110) plane of quartz on the temperature gradient applied to the crystal. Bragg angle ~90°, $L_c = 27$ cm. One can see the reflexes from the front surface and from the back part of crystal.

The scheme of the experiment for the observation of neutron spin rotation is similar to that described in [3].

To observe the effect of neutron spin rotation due to the Schwinger interaction, it is necessary to turn the
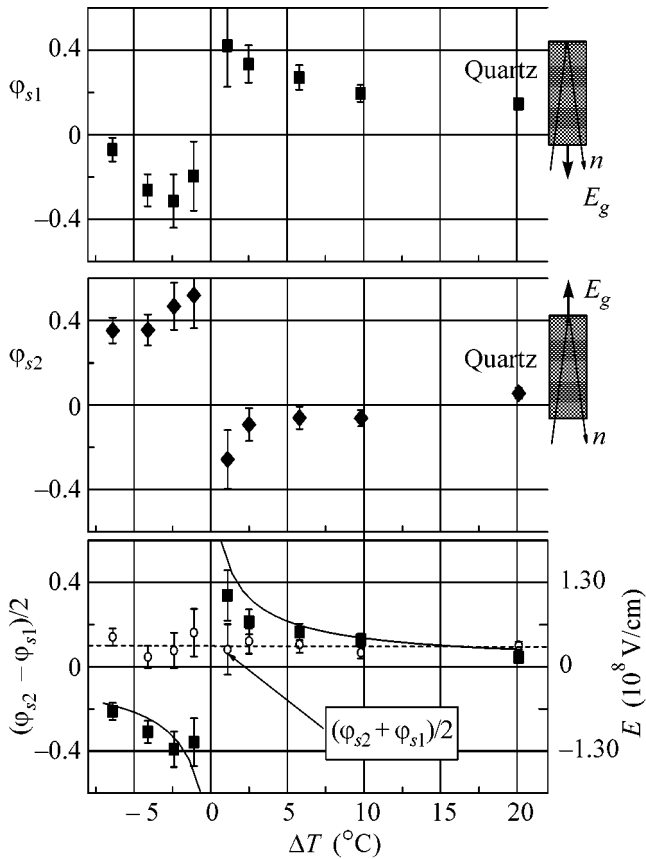
Fig. 4. The dependence of the angle of neutron spin rotation due to Schwinger interaction on the value of the temperature gradient. The two upper figures correspond to two crystal positions differing by the angle 180°. One can see a good coincidence of the theoretical dependence (solid curve in the bottom plot) with the experimental points.

crystal in a position for which Bragg angle is different from 90°, because, in the case of Bragg diffraction, the Schwinger effect disappears for a 90° Bragg angle:

$$\varphi_s = \frac{4\mathbf{E}\mu L_c v_\parallel}{c\hbar\, v_\perp} = \frac{4\mathbf{E}\mu L_c}{c\hbar}\cot(\theta_B)\xrightarrow[\theta_B \to \pi/2]{} 0 . \quad (7)$$

The experiment on the observation of neutron spin rotation was carried out with the $L_c = 14$ cm crystal thickness and Bragg angle $\approx 86°$.

The dependence of the angle of neutron spin rotation around $\mathbf{H}_S$ on the value of the temperature gradient is shown in Fig. 4.

We can change the sign of the effect by turning the crystal by the 180° around $\mathbf{H}_S$. One can see that the experiment confirms that such a crystal rotation indeed changes the sign of the observed effect. On the right axis, the effective electric field that is necessary to get the corresponding spin rotation effect is shown. One can see that the value of the electric field reaches $\sim 1.3 \times 10^8$ V/cm, which is only 1.5 times less than in the Laue diffraction case for the exact Bragg condition [5, 6].

4. CONCLUSIONS

The doubled effect of spin rotation in a noncentrosymmetric quartz crystal for neutrons Bragg reflected by the deformed part of crystal was first observed. This effect is caused by the Schwinger interaction and depends on the deformation degree of the crystal near its back surface. For the quartz crystal, the effective electric field affecting the neutron during the time of its stay inside the crystal can reach $\sim 1.3 \times 10^8$ V/cm. The sensitivity to neutron EDM is determined by the product $E\tau\sqrt{N}$, where E is the electric field affecting the neutron, τ is the time of neutron interaction with the field, and N is the total statistics accumulated in the experiment. Simple estimation has shown that, in our case, the depth of neutron penetration into the crystal and, thus, the time of neutron interaction with the electric field can be about four or even five orders more than in the well-known Shull and Nathans experiment for the neutron EDM search [14].

In addition, the requirements for the crystal perfection are relatively low for this scheme. For the case $\gamma_B \ll w_m$, the effective electric field affecting the neutron depends on an effective crystal mosaicity w_m as $E = E_0(\gamma_B/w_m)$, where γ_B is the angular Bragg width, but the reflex intensity increases as $I = I_0(w_m/\gamma_B)$; therefore, the sensitivity of measuring the neutron EDM will be reduced only by a factor $\sqrt{w_m/\gamma_B}$. This give us a hope that such a scheme can be applied to search for the T-odd part of neutron–nuclei interactions [15] using neutrons with energies near the P-wave resonance one.

REFERENCES

1. V. V. Fedorov, V. V. Voronin, E. G. Lapin, and O. I. Sumbaev, Preprint No. PNPI-1944 (Inst. of Nuclear Physics, Russian Academy of Sciences, Gatchina, 1994); Tech. Phys. Lett. **21**, 884 (1995); Physica B (Amsterdam) **234–236**, 8 (1997).

2. V. V. Fedorov, V. V. Voronin, and E. G. Lapin, Preprint No. LNPI-1644 (Inst. of Nuclear Physics, USSR Academy of Sciences, Leningrad, 1990); J. Phys. G: Nucl. Part. Phys. **18**, 1133 (1992).

3. V. V. Fedorov, E. G. Lapin, S. Yu. Semenikhin, and V. V. Voronin, Physica B (Amsterdam) **297**, 293 (2001).

4. V. V. Fedorov and V. V. Voronin, Nucl. Instrum. Methods Phys. Res. B **201**, 230 (2003).

5. V. L. Alexeev, V. V. Fedorov, E. G. Lapin, *et al.*, Nucl. Instrum. Methods Phys. Res. A **284**, 181 (1989); Sov. Phys. JETP **69**, 1083 (1989).

6. V. V. Voronin, E. G. Lapin, S. Yu. Semenikhin, and V. V. Fedorov, Preprint No. PNPI-2376 (Inst. of Nuclear Physics, Russian Academy of Sciences, Gatchina, 2000); JETP Lett. **72**, 308 (2000).

7. V. V. Voronin, E. G. Lapin, S. Yu. Semenikhin, and V. V. Fedorov, JETP Lett. **71**, 76 (2000); Preprint No. PNPI-2337 (Inst. of Nuclear Physics, Russian Academy of Sciences, Gatchina, 2000).

8. M. Forte, J. Phys. G: Nucl. Phys. **9**, 745 (1983).

9. V. G. Baryshevskii and S. V. Cherepitsa, Phys. Status Solidi B **128**, 379 (1985).

10. V. V. Fedorov *et al.*, ILL Experimental Report, Test-731 (2002).

11. M. Forte and C. M. E. Zeyen, Nucl. Instrum. Methods Phys. Res. A **284**, 147 (1989).

12. V. V. Fedorov, in *Proceedings of XXVI Winter LNPI School* (Leningrad, 1991), Vol. 1.

13. V. V. Voronin, E. G. Lapin, S. Yu. Semenikhin, and V. V. Fedorov, JETP Lett. **74**, 251 (2001).

14. C. G. Shull and R. Nathans, Phys. Rev. Lett. **19**, 384 (1967).

15. V. G. Baryshevsky, J. Phys. G: Nucl. Part. Phys. **23**, 509 (1997).

Manifestation of Geometric Effects in Temperature Behavior of AC Magnetic Response of Josephson Junction Arrays[¶]

S. Sergeenkov[1, 2] and F. M. Araujo-Moreira[1]

*[1] Departamento de Física e Engenharia Física, Grupo de Materiais e Dispositivos,
Centro Multidisciplinar para o Desenvolvimento de Materiais Cerâmicos, Universidade Federal de São Carlos,
SP, 13565-905 São Carlos, Brazil*

*[2] Bogoliubov Laboratory of Theoretical Physics, Joint Institute for Nuclear Research,
Dubna, Moscow region, 141980 Russia*

Received September 23, 2004

By improving the resolution of a homemade mutual-inductance measurement technique, a pronounced steplike structure (with the number of steps $n = 4$ for all ac fields) has been observed in the temperature dependence of ac susceptibility in artificially prepared two-dimensional Josephson junction arrays (2D-JJA) of unshunted Nb–AlO$_x$–Nb junctions with $\beta_L(4.2 \text{ K}) = 30$. Using a single-plaquette approximation of the overdamped 2D-JJA model, we were able to successfully fit our data assuming that the steps are related to the geometric properties of the plaquette. The number of steps n corresponds to the number of flux quanta that can be screened by the maximum critical current of the junctions. The steps are predicted to manifest themselves in arrays with the inductance-related parameter $\beta_L(T)$ matching a "quantization" condition $\beta_L(0) = 2\pi(n + 1)$. © *2004 MAIK "Nauka/Interperiodica".*

PACS numbers: 74.25.Ha; 74.50.+r; 74.80.Bj

1. INTRODUCTION

Many unusual and still not completely understood magnetic properties of Josephson junction arrays (JJAs) continue to attract the attention of both theoreticians and experimentalists alike (for recent reviews on the subject, see, e.g., [1–4] and further references therein). In particular, among the numerous spectacular phenomena recently discussed and observed in JJAs, we would like to mention the dynamic temperature reentrance of ac susceptibility [2] (closely related to the paramagnetic Meissner effect [3]) and avalanche-like magnetic field behavior of magnetization [4, 5] (closely related to self-organized criticality (SOC) [6, 7]). More specifically, using a highly sensitive SQUID magnetometer, magnetic field jumps in the magnetization curves associated with the entry and exit of avalanches of tens and hundreds of fluxons were clearly seen in SIS-type arrays [5]. Additionally, it was shown that the probability distribution of these processes is in good agreement with the SOC theory [7]. An avalanche character of flux motion was observed at temperatures at which the size of the fluxons did not exceed the size of the cell, that is, for discrete vortices. On the other hand, using a similar technique, magnetic flux avalanches were not observed in SNS-type proximity arrays [8] despite a sufficiently high value of the inductance (L)-related critical parameter $\beta_L = 2\pi LI_C/\Phi_0$ needed to satisfy the observability conditions of SOC. Instead, the observed quasihydrodynamic flux motion in the array was explained by the considerable viscosity characterizing the vortex motion through the Josephson junctions.

In this paper, we present experimental evidence for the manifestation of novel geometric effects in the magnetic response of high-quality ordered 2D-JJA. By increasing the resolution of our homemade mutual-inductance measurement technique, we were able to observe for the first time a fine, steplike structure (with the number of steps $n = 4$ for all ac fields used in our experiments) in the temperature behavior of ac susceptibility in artificially prepared 2D-JJA of unshunted Nb–AlO$_x$–Nb junctions. Using a single-plaquette approximation of the overdamped 2D-JJA model, we show that the number of steps n corresponds to the number of flux quanta that can be screened by the maximum critical current of the junctions and, as a result, steps will manifest themselves in arrays with the inductance-related parameter $\beta_L(T)$ matching a "quantization" condition $\beta_L(0) = 2\pi(n + 1)$.

2. EXPERIMENTAL RESULTS

To measure the complex ac susceptibility in our arrays with high precision, we used a homemade susceptometer based on the so-called screening method in the reflection configuration [9–11]. The experimental

---

[¶] This article was submitted by the authors in English.

system was calibrated using a high-quality niobium thin film. Previously, we showed that the calibrated output of the complex voltage in this experimental setup corresponds to the true complex ac susceptibility (for more details on the experimental technique and setups used in our study, see [2, 11]).

Measurements were performed as a function of the temperature T (for 1.5 K $< T <$ 15 K) and the amplitude of the excitation field h_{ac} (for 1 mOe $< h_{ac} <$ 10 Oe) normal to the plane of the array. The frequency of the ac field in the experiments reported here was fixed at 20 kHz. The unshunted 2D-JJAs used in the present study are formed by loops of niobium islands (with T_C = 9.25 K) linked through Nb–AlO$_x$–Nb Josephson junctions and consist of 100×150 tunnel junctions. The unit cell has a square geometry with lattice spacing $a = 46$ μm and a single junction area of 5×5 μm^2. Since the inductance of each loop is $L = \mu_0 a = 64$ pH and the critical current of each junction is I_C(4.2 K) = 150 μA, we have β_L(4.2 K) = 30. Recall that the parameter $\beta_L(T) = 2\pi L I_C(T)/\Phi_0$ (where Φ_0 is the magnetic flux quantum) is proportional to the number of flux quanta that can be screened by the maximum critical current in the junctions.

It is important to mention that the magnetic field dependence of the critical current of the array (taken at $T = 4.2$ K) on the dc magnetic field H_{dc} (parallel to the plane of the sample) exhibited [2, 11] a sharp Fraunhofer-like pattern characteristic of a single-junction response, thus proving a rather strong coherence within arrays (with negligible distribution of critical currents and sizes of the individual junctions) and, hence, the high quality of our samples.

The observed temperature dependence of the real part of ac susceptibility for different ac fields is shown in Fig. 1. A pronounced steplike structure is clearly seen at higher temperatures. The number of steps n does not depend on ac field amplitude and is equal to $n = 4$. As expected [2, 11, 12], for $h_{ac} >$ 40 mOe (when the array is in the mixed state with practically homogeneous flux distribution), the steps are accompanied by the previously observed reentrant behavior with $\chi'(T, h_{ac})$ starting to increase at low temperatures.

3. DISCUSSION

To understand the steplike behavior of the ac susceptibility observed in unshunted 2D-JJAs, in principle, one would need to analyze in detail the flux dynamics in these arrays. However, as we have previously reported [2, 11, 12], because of the well-defined periodic structure of our arrays with no visible distribution of junction sizes and critical currents, it is quite reasonable to assume that the experimental results obtained from the magnetic properties of our 2D-JJAs could be understood by analyzing the dynamics of just a single unit cell (plaquette) of the array. As we shall see, a theoretical interpretation of the experimental results pre-
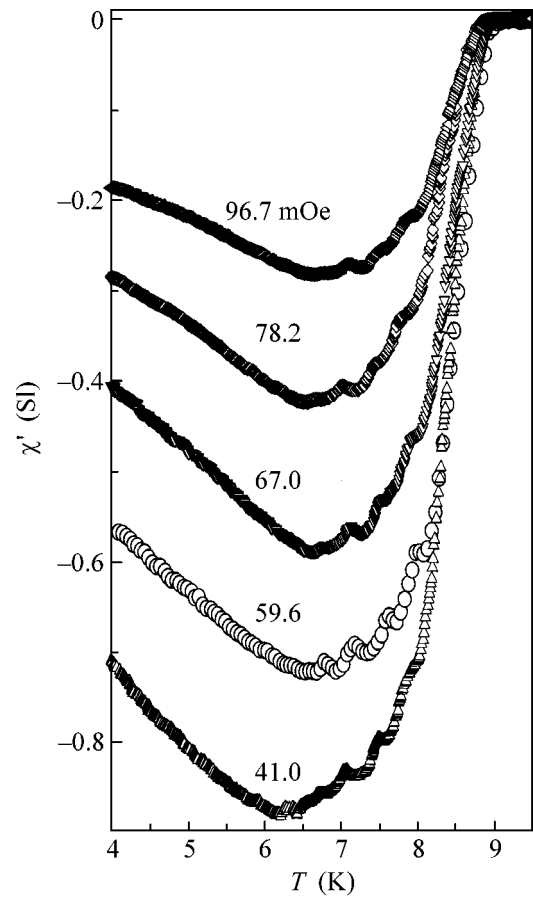

Fig. 1. Experimental results for temperature dependence of the real part of the ac susceptibility $\chi'(T, h_{ac})$ for different ac field amplitudes h_{ac} = 41.0, 59.6, 67.0, 78.2, and 96.7 mOe.

sented here based on a single-loop approximation is in excellent agreement with the observed behavior. In our analytical calculations, the unit cell is a loop containing four identical Josephson junctions and the measurements correspond to the zero-field cooling ac magnetic susceptibility. If we apply an ac external field $H_{ac}(t) = h_{ac}\cos\omega t$ normally to the 2D-JJA, then the total magnetic flux $\Phi(t)$ threading the four-junction superconducting loop is given by $\Phi(t) = \Phi_{ext}(t) + LI(t)$, where L is the loop inductance, $\Phi_{ext}(t) = SH_{ac}(t)$ is the flux related to the applied magnetic field (with $S \simeq a^2$ being the projected area of the loop), and the circulating current in the loop reads $I(t) = I_C(T)\sin\phi(t)$. Here, $\phi(t)$ is the gauge-invariant superconducting phase difference across the ith junction. As is well known, in the case of four junctions, the flux quantization condition reads [11, 13]

$$\phi = \frac{\pi}{2}\left(n + \frac{\Phi}{\Phi_0}\right), \qquad (1)$$

where n is an integer, and, for simplicity, we assume as usual that $\phi_1 = \phi_2 = \phi_3 = \phi_4 \equiv \phi$ [2, 11].
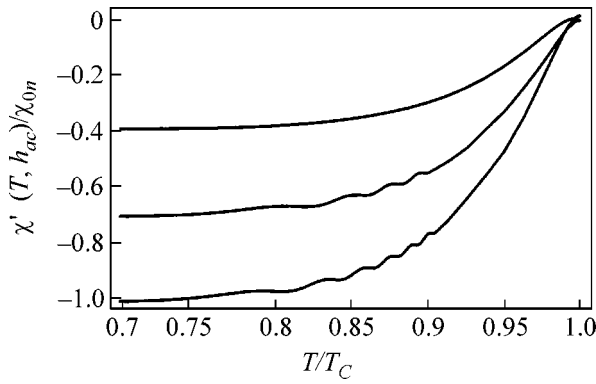
Fig. 2. Theoretically predicted dependence of the normalized susceptibility $\chi'(T, h_{ac})/\chi_{0n}$ (for better visual effect, the curves are normalized differently with $\chi_{00} = 2.5\chi_0$, $\chi_{03} = 1.5\chi_0$, and $\chi_{05} = \chi_0$, where $\chi_0 = S^2/VL$) on reduced temperature T/T_C according to Eqs. (3)–(5) for $f = 0.5$ and for "quantized" values of $\beta_L(0) = 2\pi(n + 1)$ (from top to bottom): $n = 0$, 3, and 5.

To properly treat the magnetic properties of the system, let us introduce the following Hamiltonian

$$\mathcal{H}(t) = J(T)[1 - \cos\phi(t)] + \frac{1}{2}LI^2(t), \qquad (2)$$

which describes the tunneling (first term) and inductive (second term) contributions to the total energy of a single plaquette. Here, $J(T) = (\Phi_0/2\pi)I_C(T)$ is the Josephson coupling energy.

Before turning to the interpretation of the observed steplike structure of $\chi'(T, h_{ac})$, we would like to briefly comment on the origin of reentrant behavior in our unshunted arrays (which has been previously discussed in much detail; see [2, 12]). A comparative study of the magnetic properties of two-dimensional arrays of both unshunted and shunted (using a molybdenum shunt resistor short-circuiting each junction) Nb–AlO$_x$–Nb junctions revealed [12] that the dynamic reentrance phenomenon can be explained by properly addressing the (neglected in our overdamped model) damping effects associated with the finite value of the Stewart–McCumber parameter $\beta_C(T) = 2\pi C_J R_J^2 I_C(T)/\Phi_0$ (where C_J is the capacitance and R_J is the quasiparticle resistance of the array). More precisely, the reentrance was found to take place in the unshunted arrays considered here (with $\beta_C(4.2 \text{ K}) = 30$) and totally disappeared in shunted arrays (with $\beta_C(4.2 \text{ K}) = 1$). It is important to mention that both arrays had the same value of the β_L parameter, namely, $\beta_L(4.2 \text{ K}) = 30$.

Returning to the discussion of the geometrical effects observed here, we notice that the number of observed steps n (in our case, $n = 4$) clearly hints at a possible connection between the phenomenon observed here and the flux quantization condition within a single four-junction plaquette. Indeed, the cur-

rent $I(t) = I_C(T)\sin\phi(t)$ circulating in the loop passes through its maximum value whenever $\phi(t)$ reaches the value of $\frac{\pi}{2}(2n + 1)$ with $n = 0, 1, 2, \ldots$. As a result, the maximum number of fluxons threading a single plaquette (see Eq. (1)) over the period $2\pi/\omega$ becomes equal to $\langle\Phi(t)\rangle = (n + 1)\Phi_0$. In turn, the latter equation is equivalent to the following condition: $\beta_L(T) = 2\pi(n + 1)$. Since this formula is valid for any temperature, we can rewrite it as a geometrical "quantization" condition $\beta_L(0) = 2\pi(n + 1)$. Recall that, in our array, $\beta_L(0) = 31.6$ (extrapolated from its experimental value $\beta_L(4.2 \text{ K}) = 30$), which is a perfect match for the above "quantization" condition predicting $n = 4$ for the number of steps in a single plaquette, in excellent agreement with the observations.

Based on the above discussion, we conclude that, in order to reproduce the observed temperature steps in the behavior of ac susceptibility, we need a particular solution to Eq. (1) for the phase difference in the form of $\phi_n(t) = \frac{\pi}{2}(2n + 1) + \delta\phi(t)$, assuming $\delta\phi(t) \ll 1$. After substituting this ansatz into Eq. (1), we find that

$$\phi_n(t) \simeq \frac{\pi}{2}n + \frac{1}{4}\beta_L(T) + \frac{1}{4}f\cos\omega t, \quad f = 2\pi Sh_{ac}/\Phi_0$$

is the ac-field-related frustration parameter. Using this effective phase difference, we can calculate the ac response of a single plaquette. Namely, the real part of susceptibility reads

$$\chi'(T, h_{ac}) = \frac{1}{\pi}\int_0^\pi d(\omega t)\cos(\omega t)\chi_n(t), \qquad (3)$$

where

$$\chi_n(t) = -\frac{1}{V}\left[\frac{\partial^2 \mathcal{H}}{\partial h_{ac}^2}\right]_{\phi = \phi_n(t)}. \qquad (4)$$

Here, V is the sample volume.

For the explicit temperature dependence of $\beta_L(T) = 2\pi LI_C(T)/\Phi_0$, we use the well-known [14, 15] analytical approximation of the BCS gap parameter (valid for all temperatures): $\Delta(T) = \Delta(0)\tanh\left(2.2\sqrt{\frac{T_C - T}{T}}\right)$, with $\Delta(0) = 1.76k_BT_C$, which governs the temperature dependence of the Josephson critical current

$$I_C(T) = I_C(0)\left[\frac{\Delta(T)}{\Delta(0)}\right]\tanh\left[\frac{\Delta(T)}{2k_BT}\right]. \qquad (5)$$

Figure 2 depicts the dependence of the ac susceptibility on reduced temperature predicted by Eqs. (3)–(5) for $f = 0.5$ and for different "quantized" values of $\beta_L(0) = 2\pi(n + 1)$. Notice the appearance of three and five steps
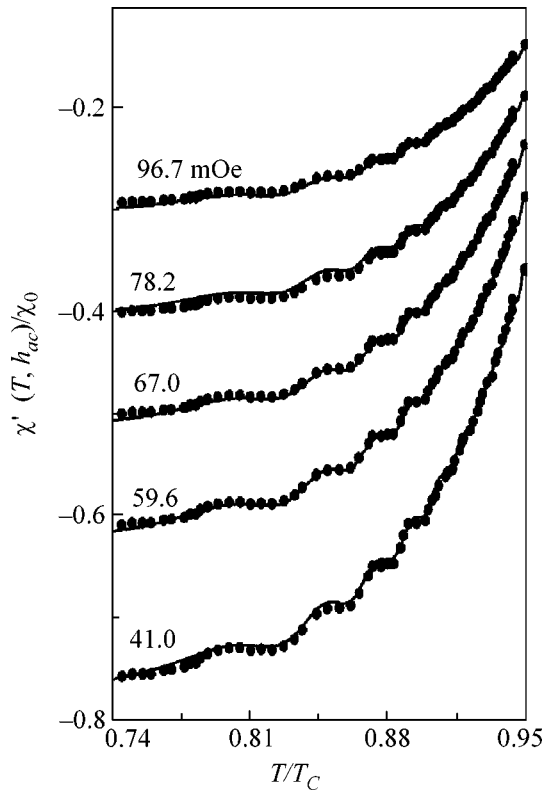
Fig. 3. Fits (solid lines) of the experimental data for $h_{ac} =$ 41.0, 59.6, 67.0, 78.2, and 96.7 mOe according to Eqs. (3)–(5) with $\beta_L(0) = 10\pi$.

for $n = 3$ and $n = 5$, respectively (as expected, the case $n = 0$ corresponds to a smooth temperature behavior without steps).

In Fig. 3, we present fits (shown by solid lines) of the observed temperature dependence of the normalized susceptibility $\chi'(T, h_{ac})/\chi_0$ for different magnetic fields h_{ac} according to Eqs. (3)–(5) using $\beta_L(0) = 10\pi$. As is seen, our simplified model based on a single-plaquette approximation demonstrates an excellent agreement with the observations.

In summary, a steplike structure (accompanied by previously seen low-temperature reentrance phenomenon) has been observed for the first time in the temperature dependence of ac susceptibility in artificially prepared two-dimensional Josephson junction arrays of unshunted Nb–AlO$_x$–Nb junctions. The steps are shown to occur in arrays with the inductance-related

parameter $\beta_L(T)$ matching the "quantization" condition $\beta_L(0) = 2\pi(n + 1)$, where n is the number of steps.

REFERENCES

1. R. S. Newrock, C. J. Lobb, U. Geigenmuller, and M. Octavio, Solid State Phys. **54**, 263 (2000); *Mesoscopic and Strongly Correlated Electron Systems-II*, Ed. by M. V. Feigel'man, V. V. Ryazanov, and V. B. Timofeev; Phys. Usp. (Suppl.) **44** (10) (2001); S. Sergeenkov, in *Studies of High Temperature Superconductors*, Ed. by A. V. Narlikar (Nova Sci., New York, 2001), Vol. 39, p. 117.

2. F. M. Araujo-Moreira, P. Barbara, A. B. Cawthorne, and C. J. Lobb, in *Studies of High Temperature Superconductors*, Ed. by A. V. Narlikar (Nova Sci., New York, 2002), Vol. 43, p. 227.

3. M. S. Li, Phys. Rep. **376**, 133 (2003).

4. E. Altshuler and T. H. Johansen, Rev. Mod. Phys. **76**, 471 (2004).

5. S. M. Ishikaev, E. V. Matizen, V. V. Ryazanov, *et al.*, JETP Lett. **72**, 26 (2000).

6. H. J. Jensen, *Self Organized Criticality: Emergent Complex Behavior in Physical and Biological Systems* (Cambridge Univ. Press, Cambridge, 1998).

7. S. L. Ginzburg and N. E. Savitskaya, JETP Lett. **73**, 145 (2001).

8. S. M. Ishikaev, E. V. Matizen, V. V. Ryazanov, and V. A. Oboznov, JETP Lett. **76**, 160 (2002).

9. B. Jeanneret, J. L. Gavilano, G. A. Racine, *et al.*, Appl. Phys. Lett. **55**, 2336 (1989).

10. P. Martinoli and C. Leeman, J. Low Temp. Phys. **118**, 699 (2000).

11. F. M. Araujo-Moreira, P. Barbara, A. B. Cawthorne, and C. J. Lobb, Phys. Rev. Lett. **78**, 4625 (1997); P. Barbara, F. M. Araujo-Moreira, A. B. Cawthorne, and C. J. Lobb, Phys. Rev. B **60**, 7489 (1999).

12. F. M. Araujo-Moreira, W. Maluf, and S. Sergeenkov (unpublished).

13. A. Barone and G. Paterno, *Physics and Applications of the Josephson Effect* (Wiley, New York, 1982; Mir, Moscow, 1984).

14. R. Meservey and B. B. Schwartz, in *Superconductivity*, Ed. by R. D. Parks (Marcel Dekker, New York, 1969), Vol. 1, p. 117.

15. S. Sergeenkov, JETP Lett. **76**, 170 (2002).

Zero-energy Andreev Surface Bound States in the Lattice Model[¶]

A. M. Bobkov

Institute of Solid-State Physics, Russian Academy of Sciences, Chernogolovka, Moscow region, 142432 Russia
e-mail: bobkov@issp.ac.ru
Received October 4, 2004

The conditions for zero-energy Andreev surface bound states to exist are found for the lattice model of a *d*-wave superconductor with arbitrary surface orientation. Both nearest-neighbors and next-nearest-neighbors models are considered. It is shown that the results are very sensitive to the surface orientation. In particular, for a half-filled (*hl*0)-surface, zero-energy Andreev surface states only appear under the condition that *h* and *l* are odd simultaneously. © *2004 MAIK "Nauka/Interperiodica".*

PACS numbers: 74.25.Jb; 74.45.+c

Significant features of high-temperature superconductors (HTS) are zero-energy Andreev surface bound states. The zero-energy states (ZES) form on surfaces of a *d*-wave superconductor with orientations different from (100), due to the sign change of the order parameter. In high-temperature superconductors, such states manifest themselves as the zero-bias conductance peak in tunneling spectroscopy in the *ab*-plane [1–26], the anomalous temperature behavior of the Josephson critical current [27–30], and the upturn in the temperature dependence of the magnetic penetration depth [31–33]. At the same time, the problem of ZES at a surface with arbitrary orientation is still not clear.

The conventional description of Andreev surface bound states, as well as the majority of inhomogeneous superconducting problems, is based usually on the continuous quasiclassical approximation. From this viewpoint, the conditions for ZES to exist are quite simple. ZES are formed due to the changing of order parameter sign along the quasiclassical trajectory. There are no ZES for the (100) (i.e., 0°) orientation, and there are ZES at all values $k_{\parallel}$ for the (110) (45°) orientation. For intermediate surface orientations, the sign change does not take place for all incoming momentum directions, and the weight of the ZES decreases with deviation from the 45° orientation.

From the other side, the tight-binding BCS model is widely used for theoretical description of HTS. This model gives the same (as the continuous quasiclassical model) result for ZES at the (100) and (110) orientations. However, for the intermediate surface orientations, the question is very complicated. To the best of my knowledge, only the simplest orientations (100), (110), (210) [21, 23, 34–37] have been studied. And even numerical calculations could not give the general

answer for all surface orientations because of the lattice specificity.

In this paper, the general analytical criterion for zero-energy Andreev surface bound states to exist at a surface of arbitrary orientation is presented. I consider a two-dimensional tight-binding model on a square lattice. The surface orientation is assumed to be arbitrary and characterized by the indexes (*hl*0). Both nearest-neighbors and next-nearest-neighbors models are considered. For simplicity, I take the superconducting order parameter to be spatially constant. This approximation is reasonable for studying low-energy quasiparticle states. The impenetrable surface is assumed to be smooth.

The Hamiltonian for a pure singlet superconductor in the tight-binding model can be written as

$$\mathcal{H} = -\sum_{\mathbf{x}, \mathbf{x}', \sigma} t(\mathbf{x}, \mathbf{x}') c_{\sigma}^{\dagger}(\mathbf{x}) c_{\sigma}(\mathbf{x}')$$
$$+ \sum_{\mathbf{x}, \mathbf{x}'} \{ \Delta(\mathbf{x}, \mathbf{x}') c_{\uparrow}^{\dagger}(\mathbf{x}) c_{\downarrow}^{\dagger}(\mathbf{x}') + \text{h.c.} \}. \tag{1}$$

Here, $t(\mathbf{x}, \mathbf{x}) = \mu$ is the chemical potential; $t(\mathbf{x}, \mathbf{x} \pm \mathbf{a}) = t(\mathbf{x}, \mathbf{x} \pm \mathbf{b}) = t > 0$, $t(\mathbf{x}, \mathbf{x} \pm \mathbf{a} \pm \mathbf{b}) = t' \leq 0$ are the hopping elements; *d*-wave superconducting pairing is defined for nearest neighbors $\Delta(\mathbf{x}, \mathbf{x} \pm \mathbf{a}) = -\Delta(\mathbf{x}, \mathbf{x} \pm \mathbf{b}) = \Delta$. Here, $\mathbf{x}$ are the positions of lattice sites; $\mathbf{a}, \mathbf{b}$ are the basic lattice vectors. Then, the Bogoliubov–de Gennes equations take the form

$$\sum_{\mathbf{x}'} \begin{bmatrix} -t(\mathbf{x}, \mathbf{x}') & \Delta(\mathbf{x}, \mathbf{x}') \\ \Delta^*(\mathbf{x}, \mathbf{x}') & t(\mathbf{x}, \mathbf{x}') \end{bmatrix} \begin{pmatrix} u(\mathbf{x}') \\ v(\mathbf{x}') \end{pmatrix} = E \begin{pmatrix} u(\mathbf{x}) \\ v(\mathbf{x}) \end{pmatrix}. \tag{2}$$

We define new coordinates $(\hat{x}, \hat{y})$, rotated with respect to the crystal axes $(\hat{a}, \hat{b})$, where $\hat{x}$ is the direc-

---
[¶] This article was submitted by the author in English.

tion normal to the surface and $\hat{y}$ is the direction along the surface. The superconductor is situated at $x > 0$. The lattice constant is taken to be unity, $a = 1$. The system is periodic along the y direction with period $\sqrt{h^2 + l^2} \equiv d^{-1}$, and the crystal momentum component k_y of a quasiparticle is conserved. Instead of the usual square Brillouin zone (BZ) $k_a \in [-\pi, \pi]$, $k_b \in [-\pi, \pi]$, we now use the surface-adapted Brillouin zone (SABZ) [23, 36] given by $k_x \in [-\pi/d, \pi/d]$ and $k_y \in [-\pi d, \pi d]$. Here, $d = 1/\sqrt{h^2 + l^2}$ is the distance between the nearest chains (layers) aligned along the surfaces; i.e., all x coordinates have discrete values with period d. The momenta in the two-coordinate systems are simply related through rotation of an angle $\theta = \tanh^{-1} h / l$.

Let us solve Eq. (2) for a half-space $x > 0$ and fixed k_y. The general solution is constructed from all the solutions of the uniform problem that do not grow at $x \longrightarrow +\infty$. Then, the wave function for fixed k_y can be written as

$$\begin{pmatrix} u(x, k_y) \\ v(x, k_y) \end{pmatrix} = \sum_{\alpha} C_{\alpha} \begin{pmatrix} u_{\alpha}(k_y) \\ v_{\alpha}(k_y) \end{pmatrix} e^{ik_{x,\alpha}x}; \qquad (3)$$

here, summation should be taken over all solutions $k_{x,\alpha}$ of the equation

$$E^2 = \xi^2(k_x, k_y) + \Delta^2(k_x, k_y), \qquad (4)$$

with $\mathrm{Im}\, k_{x,\alpha} > 0$. The boundary conditions are

$$\begin{pmatrix} u(-jd, k_y) \\ v(-jd, k_y) \end{pmatrix} = 0, \quad j = 0, 1, ..., N-1, \qquad (5)$$

where $N = \max(h, l)$ for the nearest-neighbors model ($t \neq 0$, $t' = 0$) or $N = h + l$ for the next-nearest-neighbors model ($t, t' \neq 0$) [35]. The total number of solutions (4) with $\mathrm{Im}\, k_{x,\alpha} > 0$ equals $2N$. Some of them correspond to the intersections of the line $k_y = $ const with the Fermi surface and have a small imaginary part of $k_{x,\alpha}$; the others correspond to the point with $(\mathrm{Re}\, k_{x,\alpha}, k_y)$ far from the Fermi surface. Therefore, we obtain from (5) the system of $2N$ linear equations for constants C_{α} with E as a parameter. Then, the equality of the determinant of the system to zero is the condition for the existence of bound states with energy E:

$$\mathrm{Det} \begin{pmatrix} u_1 & \cdots & u_{2N} \\ v_1 & \cdots & v_{2N} \\ u_1 e^{ik_{x,1}d} & \cdots & u_{2N}e^{ik_{x,2N}d} \\ \cdots & \cdots & \cdots \\ v_1 e^{ik_{x,1}(N-1)d} & \cdots & v_{2N}e^{ik_{x,2N}(N-1)d} \end{pmatrix} = 0. \quad (6)$$

We only consider now the possibility for dispersionless states with $E = 0$ to exist in some region of k_y. Then, all the solutions of (4) have the form $(u_{\alpha}(k_y), v_{\alpha}(k_y))^T = (1, -i\rho_{\alpha})$ with $\rho_{\alpha} = \pm 1$. From each point of intersection $k_y = $ const with the Fermi surface, we obtain one solution with $\rho_{\alpha} = \mathrm{sgn}(v_{f,x}(k_{x,f}, k_y)\Delta(k_{x,f}, k_y))$ in the quasiclassical approximation. And from each point far from the Fermi surface, we obtain two solutions with close values of k_x and with opposite values of ρ_{α}.

Let n and m be numbers of solutions corresponding to $\rho_{\alpha} = \pm 1$, respectively. Then, we can obtain after some straightforward algebra that, in the case of $n \neq m$, Eq. (6) is always true. For $n = m$, Eq. (6) can be reduced to

$$\prod_{\rho = -1, i < j} (k_{x,i} - k_{x,j}) \prod_{\rho = +1, i < j} (k_{x,i} - k_{x,j}) = 0. \qquad (7)$$

The wavevectors $k_{x,\alpha}$ corresponding to the same sign of ρ_{α} can only coincide for a few values of k_y, for which different parts or Fermi surfaces intersect with each other. Therefore, we obtain the simple criterion for dispersionless zero-energy bound states to exist: $n \neq m$. Since the solutions corresponding to the values of $\mathbf{k}$ that are situated far from the Fermi surface always appear in pairs with opposite signs of ρ_{α}, we can safely take into account only solutions with $\mathbf{k}$ defined by the intersections of the line $k_y = $ const with the Fermi surface.

Let us apply this criterion to the model under consideration. In the quasiclassical approximation, we need to obtain all intersections of the line $k_y = $ const with the Fermi surface in SABZ and, then, calculate $\rho = \mathrm{sgn}(v_{f,x}(\mathbf{k})\Delta(\mathbf{k}))$ for all these points. Let us consider all values of k_y simultaneously and find the positions of the edges of the regions where zero-energy surface states exist.

Due to the symmetry of the normal metal quasiparticle energy spectrum and the superconducting gap to the inversion $\xi(\mathbf{k}) = \xi(-\mathbf{k})$, $\Delta(\mathbf{k}) = \Delta(-\mathbf{k})$, we need to consider only points at the Fermi surface where the sign of ρ changes. They are the points of the gap sign changing and the points of v_x sign changing.

It is easy to show that points of v_x sign changing cannot modify the parameters n and m. These points are the tangent points of the Fermi surface and the line $k_y = $ const. On the one side (along the k_y axis) from the point of v_x sign changing, there are two solutions with opposite signs of ρ_{α}. On the other side from this point, there are no real solutions, but there are two solutions that have large imaginary parts of k_x and opposite signs of ρ_{α} as well.

Thus, let us consider only points of gap sign changing. We should take into account the univocal correspondence of the SABZ and the usual first BZ. Then, there are only four points of gap sign changing in SABZ, just as in BZ: $(k_a^0, k_b^0) = (\pm v\pi, \pm v\pi)$ in the crys-
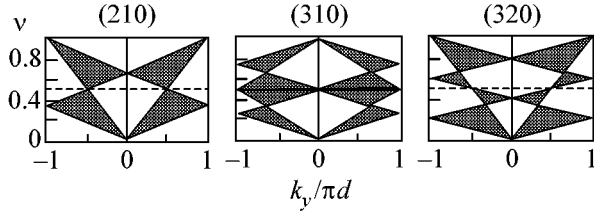
Grey—regions of ZES existence in the (k_y, ν) plane. Black lines are the lines of zero gap. The dashed line corresponds to half-filling $\mu = 0$. The parameter $\nu = \pi^{-1} \arccos(-\mu/4t)$ for nearest-neighbors model and $\nu = \pi^{-1} \arccos(-\mu/2 \, (t + \sqrt{t^2 - t'\mu}\,))$ for the next-nearest-neighbors model.

tal axes. Here, the parameter ν takes the value $\pi^{-1} \arccos(-\mu/4t)$ for the nearest-neighbors model and

$$\nu = \pi^{-1} \arccos\left(\frac{-\mu}{2(t + \sqrt{t^2 - t'\mu})}\right) \tag{8}$$

for the more general case of the next-nearest-neighbors model. Parameter ν is a relative coordinate of a BZ point where the gap sign changing takes place and is correlated with the filling of the band. The maximal and minimal values of ν are 0 and 1. For the simplest case of half-filling ($\mu = 0$), we get $\nu = 1/2$. But ν is not strictly the filling of the band.

Now, we need to obtain the coordinates k_y^0 of the gap sign-changing points in SABZ. For the $(hl0)$ orientation,

$$k_y^0 = -k_a^0 \frac{l}{\sqrt{h^2 + l^2}} + k_b^0 \frac{h}{\sqrt{h^2 + l^2}}; \tag{9}$$

then, for k_y^0-coordinates of four gap sign changing points,

$$k_y^0 = (\pm h \pm l)\pi\nu d. \tag{10}$$

Since k_y is a crystal momentum, one can move the k_y^0 coordinates of these points into the SABZ. Finally, we obtain the following regions of k_y where ZES exist:

$$\left|k_y^0\right| \in (k_{\min}, k_{\max}), \tag{11}$$

where

$$k_{\min} = \min\{|F[(h-l)\pi\nu d]|, |F[(h+l)\pi\nu d]|\}, \tag{12}$$

$$k_{\max} = \max\{|F[(h-l)\pi\nu d]|, |F[(h+l)\pi\nu d]|\}. \tag{13}$$

Here, $F[...]$ is a function that shifts the argument to the permissible for a SABZ value: $F[k_y] = (\{(1/2) + (k_y/2\pi d)\} - (1/2))2\pi d$; $\{...\}$ is a fractional part of the argument. From Eq. (11), we can see that the region of k_y where zero-energy bound states take place always exists, except for the case of

$$k_{\min} = k_{\max}. \tag{14}$$

It is easy to obtain from Eqs. (11)–(13) the regions of ZES existence for any case under consideration. In the figure, results for (210), (310), and (320) surfaces are shown. It is important to note that regions with ZES and regions without them are separated by the lines of zero gap (for these values of k_y, the superconducting gap vanishes for one of the quasiparticle trajectories forming the state).

For a half-filled $(hl0)$ surface, the result can be formulated in a general form: zero-energy Andreev surface states appear only for the case of odd h and l. Moreover, it is seen from (14) that, for any surface orientation, one can find a set of values of ν for which there are no zero energy states. From (14), we have $h + l$ values of ν (and the same number of band fillings):

$$\nu = i/l, \, j/h, \quad i = 1, ..., h-1, \quad j = 1, ..., l-1. \tag{15}$$

The conditions for a zero-energy Andreev surface bound state to exist are studied for the lattice model of a d-wave superconductor. An arbitrary surface orientation is considered for the nearest-neighbors as well as for the next-nearest-neighbors model. The result is very sensitive to the surface orientation and does not change continuously under surface-to-crystal angle rotation. In particular, for a half-filled $(hl0)$ surface, zero-energy Andreev surface states only appear under the condition that h and l are odd simultaneously.

REFERENCES

1. J. Geerk, X. Xi, and G. Linker, Z. Phys. B **73**, 329 (1988).

2. C.-R. Hu, Phys. Rev. Lett. **72**, 1526 (1994).

3. Y. Tanaka and S. Kashiwaya, Phys. Rev. Lett. **74**, 3451 (1995).

4. M. Matsumoto and H. Shiba, J. Phys. Soc. Jpn. **64**, 1703 (1995); **64**, 3384 (1995); **64**, 4867 (1995); **65**, 2194 (1996).

5. L. J. Buchholtz, M. Palumbo, D. Rainer, and J. A. Sauls, J. Low Temp. Phys. **101**, 1079 (1995); **101**, 1099 (1995).

6. S. Kashiwaya, Y. Tanaka, M. Koyanagi, *et al.*, Phys. Rev. B **51**, 1350 (1995).

7. M. Covington, R. Scheuerer, K. Bloom, and L. H. Greene, Appl. Phys. Lett. **68**, 1717 (1996).

8. J. H. Xu, J. H. Miller, Jr., and C. S. Ting, Phys. Rev. B **53**, 3604 (1996).

9. M. Fogelström, D. Rainer, and J. A. Sauls, Phys. Rev. Lett. **79**, 281 (1997).

10. Yu. Barash, H. Burkhardt, and A. Svidzinsky, Phys. Rev. B **55**, 15282 (1997).

11. M. Covington, M. Aprili, E. Paraoanu, *et al.*, Phys. Rev. Lett. **79**, 277 (1997).

12. L. Alff, H. Takashima, S. Kashiwaya, *et al.*, Phys. Rev. B **55**, R14757 (1997).

13. J. W. Ekin, Y. Xu, S. Mao, *et al.*, Phys. Rev. B **56**, 13746 (1997).

14. M. Aprili, M. Covington, E. Paraoanu, *et al.*, Phys. Rev. B **57**, R8139 (1998).

15. L. Alff, S. Kleefisch, U. Schoop, *et al.*, Eur. Phys. J. B **5**, 423 (1998).

16. L. Alff, A. Beck, R. Gross, *et al.*, Phys. Rev. B **58**, 11197 (1998).

17. S. Sinha and K.-W. Ng, Phys. Rev. Lett. **80**, 1296 (1998).

18. J. Y. T. Wei, N.-C. Yeh, D. F. Garrigus, and M. Strasik, Phys. Rev. Lett. **81**, 2542 (1998).

19. M. Aprili, E. Badica, and L. H. Greene, Phys. Rev. Lett. **83**, 4630 (1999).

20. R. Krupke and G. Deutscher, Phys. Rev. Lett. **83**, 4634 (1999).

21. J.-X. Zhu, B. Friedman, and C. S. Ting, Phys. Rev. B **59**, 3353 (1999).

22. M. Covington and L. H. Greene, Phys. Rev. B **62**, 12440 (2000).

23. P. Pairor and M. B. Walker, Phys. Rev. B **65**, 064507 (2002).

24. H. Aubin, L. H. Greene, Sha Jian, and D. G. Hinks, Phys. Rev. Lett. **89**, 177001 (2002).

25. Shin-Tza Wu and Chung-Yu Mou, Phys. Rev. B **67**, 024503 (2003).

26. L. H. Green, P. Hentges, H. Aubin, *et al.*, Physica C (Amsterdam) **387**, 162 (2003).

27. Y. Tanaka and S. Kashiwaya, Phys. Rev. B **53**, 11957 (1996).

28. Yu. S. Barash, H. Burkhardt, and D. Rainer, Phys. Rev. Lett. **77**, 4070 (1996).

29. E. Il'ichev, M. Grajcar, R. Hlubina, *et al.*, Phys. Rev. Lett. **86**, 5369 (2001).

30. G. Testa, A. Monaco, E. Esposito, *et al.*, cond-mat/0310727.

31. H. Walter, W. Prusseit, R. Semerad, *et al.*, Phys. Rev. Lett. **80**, 3598 (1998).

32. Yu. S. Barash, M. S. Kalenkov, and J. Kurkijärvi, Phys. Rev. B **62**, 6665 (2000).

33. A. Carrington, F. Manzano, R. Prozorov, *et al.*, Phys. Rev. Lett. **86**, 1074 (2001).

34. Y. Tanuma, Y. Tanaka, M. Ogata, and S. Kashiwaya, Phys. Rev. B **60**, 9817 (1999).

35. A. M. Bobkov, L.-Y. Zhu, S.-W. Tsai, *et al.*, Phys. Rev. B **70**, 144502 (2004).

36. M. B. Walker and P. Pairor, Phys. Rev. B **59**, 1421 (1999).

37. S. Kashiwaya and Y. Tanaka, Rep. Prog. Phys. **63**, 1641 (2000).

Coherent Scattering in a Small Quantum Dot

V. A. Tkachenko[1, *], O. A. Tkachenko[1, 2, 3], Z. D. Kvon[1, 2], D. G. Baksheev[1],
A. L. Aseev[1], and J. C. Portal[3]

[1] *Institute of Semiconductor Physics, Siberian Division, Russian Academy of Sciences,*
pr. Akademika Lavrent'eva 13, Novosibirsk, 630090 Russia
[2] *Novosibirsk State University, ul. Pirogova 2, Novosibirsk, 630090 Russia*
[3] *Grenoble High Magnetic Fields Laboratory, MPI-FKF and CNRS, B.P. 166, F-38042 Grenoble, France*
* *e-mail: vtkach@isp.nsc.ru*
Received October 4, 2004

Ballistic transport in an open small (100 nm) three-terminal quantum dot has been analyzed. The dot is based on the high-mobility 2D electron gas of the AlGaAs/GaAs heterojunction. It has been shown that the gate oscillations of the resistance of such a dot arise due to the coherent scattering of electrons on its quasidiscrete levels and these oscillations are suppressed by a weak magnetic field. © *2004 MAIK "Nauka/Interperiodica".*

PACS numbers: 73.23.Ad; 73.50.–h

Quantum scattering in systems with a short-range confining potential is a classical quantum-mechanical problem. In one-dimensional and spherically symmetric potentials, resonances with respect to the energy of the incident particles arise at the energies corresponding to quasilevels. Moreover, the approach of a real or virtual level to the continuum bottom is accompanied by a sharp change in the scattering phase of low-energy particles and, hence, by resonance effects [1]. Experimental investigation of quantum scattering is obviously an interesting problem of the physics of low-dimensional systems. The corresponding experiments have already been carried out for superlattice structures. In particular, transport resonances caused by the transformation of levels to virtual ones at the boundary between *p*-GaAs with the Stark AlAs/GaAs superlattice were recently detected [2]. It appeared to be more difficult to observe resonance-scattering effects in lateral submicron systems. This is associated with a narrow spacing between quasilevels and mesoscopic fluctuations of conductance. In particular, the theoretical models of devices made of 1D quantum wires predicted regular large-amplitude oscillations in conductance [3]. However, the frequent gate oscillations associated with longitudinal quantization were much weaker in experiments [4]. Such a problem arose in experiments with lateral multielectron quantum dots, where the oscillations of conductance in the open state are random and mesoscopic [5].

Recently, we studied the splitting points of 1D quantum channels in nanostructures created on heterojunctions with a 2D electron gas [6–9]. According to the calculations of 3D electrostatics and 2D transport, these dots are small (~100 nm) and of a triangular shape, and they must provide well-resolved high-amplitude oscillations of penetrability, which are caused by the coher-

ent scattering on the quasilevels of the dot [6, 9]. In this work, this prediction is experimentally verified for a single quantum dot located between three close antidots [7, 8]. We report the results of new measurements and calculations that corroborate the interference nature of observed effects caused by scattering on the quasilevels of the open dot.

Quantum dots were manufactured on the basis of a 2D electron gas in the AlGaAs/GaAs heterojunction with a mobility of $\mu = 3 \times 10^5$ cm^2/V s and an electron density of $n = 3 \times 10^{11}$ cm^{-2}. Dots are small triangular sections of the 2D electron gas between three antidots located in the vertices of a 400-nm-side triangle. Antidots and isolating cuts to them were produced by electron lithography and subsequent plasmochemical etching. The final operation was the deposition of a metallic TiAu gate. Structural data, along with a numerical simulation of the 3D electrostatics of such devices, were presented in [8], where it was shown that the triangular dot under investigation in the tunneling regime acted as a single-electron transistor.

The resistances of these devices in the open regime were measured in a temperature range of 40 mK–1.5 K by the use of the four-point scheme at a frequency of 7.5 Hz in a current range of 0.1–1 nA. The current $I = I_{ij}$ was specified, and we measured the ratios $R_{ijkl} = V_{kl}/I_{ij}$, where the reservoir numbers i, j, k, and l vary from 1 to 3 and V_{kl} is the voltage. In most samples, the cuts that form the antidots in the 2D electron gas are insulators between three reservoirs. For other samples, contacts 2 and 3 on one Hall bridge led to the common reservoir ($V_{12} = V_{13} = V$). The total dot conductance $G = I/V$ was measured in this case.

Figure 1 shows the experimental results for three and two isolated reservoirs and various cool-downs for

one of the samples. It is seen that qualitatively similar oscillations in these cases are observed in the gate dependence of the corresponding inverse resistances $R_{1213}^{-1}(V_g)$ (Fig. 1a) and $G(V_g)$ (Fig. 1b) in the absence of a magnetic field. Oscillations are observed against the background of two plateaus with conductance values $2e^2/h$ and $4e^2/h$. For $B = 0$, the deep dips near the first plateau with a characteristic spacing of $\Delta V_g = 20$–25 meV between them are most regular and reproducible.

The doublet splitting of the peaks is observed in one case (Fig. 1a, line 2, $T = 0.1$ K). The fine structure of the oscillations that is found in the experiment is inconsistent with the previous interpretation of the oscillations as a result of the addition of one electron to the dot [7]. Single-electron oscillations must have a period of $\Delta V_g = e/C_g$, where e is the elementary charge and C_g is the gate capacity of the dot. These oscillations have the form of simple peaks and (very rarely) Fano resonances (peak–dip) [10]. The structure of the oscillations is more complex in the case under consideration. Moreover, simple oscillations are replaced by complex oscillations upon a recurrent immersion of the same sample in a cryostat, when the nature of transport and C_g cannot significantly change. It is known that the gate capacity is not a mesoscopic parameter [9, 11]. At the same time, according to Fig. 1, our oscillations are of a mesoscopic nature, when the switch of the charge state of impurities upon a recurrent process of cooling the sample can change the form of the oscillations and their period. The observed transformations of the lines upon the transition to another mesoscopic state can be attributed to the response of quantum interference to a change in the potential shape [8, 9], which leads to the shifts of single-particle quasilevels and to the corresponding change in scattering on these levels. This explanation is consistent with our experimental results (Fig. 1) and calculation of the gate capacity of the dot under investigation. We obtain $C_g = 5.1 \times 10^{-17}$ F from the solution of the 3D electrostatic problem.

The agreement between calculations of the capacity and experiment was tested in the Coulomb-blockade regime. In this regime, one of the contacts of the dot was completely closed, and the corresponding reservoir of the 2D electron gas was a side gate. Conductance as a function of the voltage on the side gate V_{jg} exhibits single-electron peaks with a period of $\Delta V_{jg} = 20$ mV. According to the 3D electrostatic calculation, the capacity of the dot with respect to the side gate is equal to $C_{jg} = 0.8 \times 10^{-17}$ F; i.e., the measured ΔV_{jg} value coincides with e/C_{jg} [8].

Oscillations of another type were observed in the open regime (Fig. 1), although ΔV_g accidentally turned out to be close to ΔV_{jg}. In particular, if $\Delta V_g \approx 25$ mV, then $\Delta V_g \approx 8e/C_g$; i.e., the occupation of four spin-degenerate single-particle levels of the dot is required for the transition to the next oscillation of resistance.
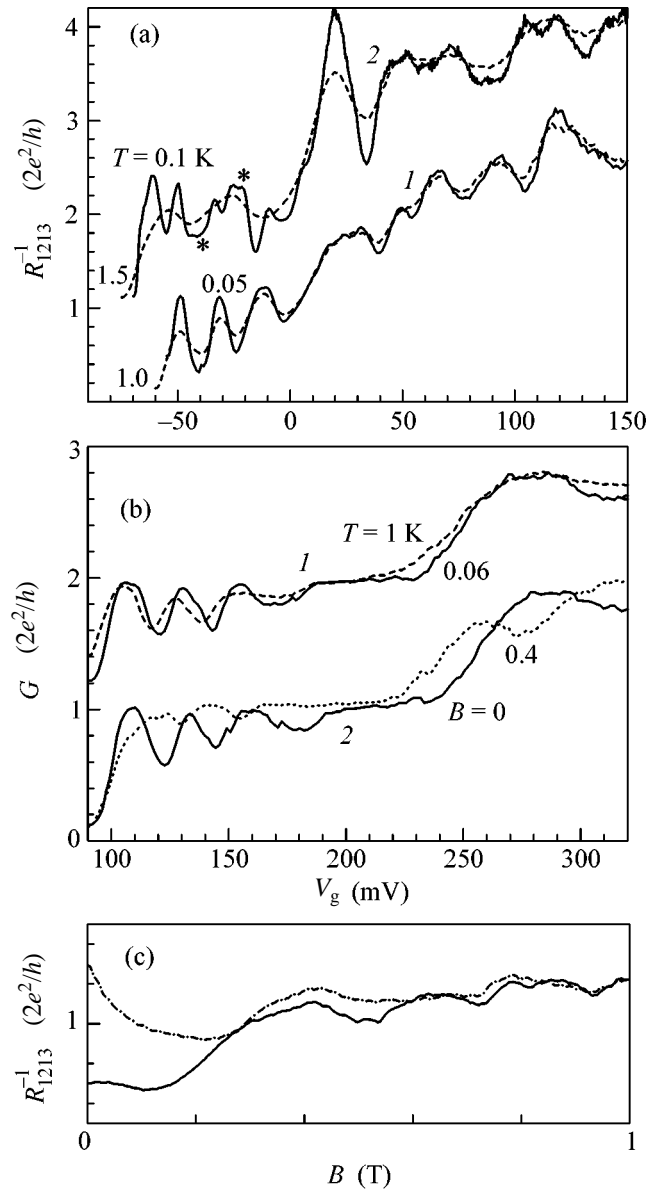

Fig. 1. (a) Inverse resistances $R_{1213}^{-1}(V_g)$ of the three-terminal quantum dot for the indicated temperatures T and two mesoscopic states 1 and 2 (lines are shifted along the ordinate axis by $2e^2/h$); (b) total conductance of the quantum dot vs. the gate voltage (two terminals from the dot lead to the common reservoir), and the effect of the magnetic field B is shown for case 2 ($T = 0.04$ K); and (c) magnetic-field dependence of R_{1213}^{-1} of the three-terminal dot for V_g values marked by the asterisks in panel (a).

Therefore, each such level needs not to necessarily provide an individual resonance in scattering. This situation is known for spherically symmetric potentials [1], and it was previously realized in the experiments with sufficiently small two-terminal quantum dots [11–13]. In the case under consideration, it can be supposed that the levels providing unsplit oscillations are doubly
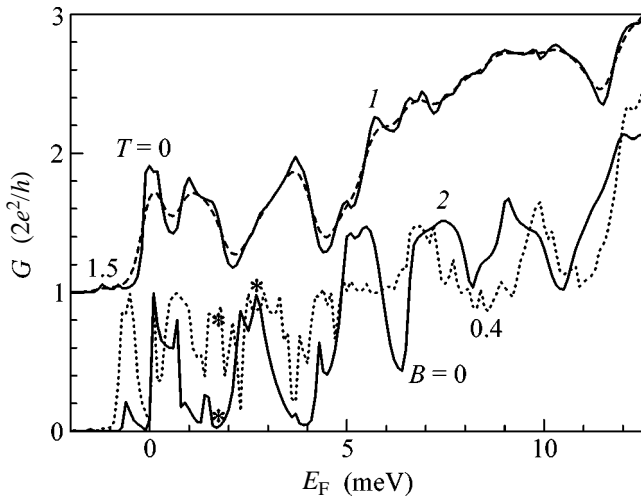
Fig. 2. Total conductance of the quantum dot vs. the Fermi energy for slightly different potential profiles *1* and *2* (lines *2* correspond to the less open and more asymmetric dot). The lines for case *1* ($B = 0$) are shifted along the ordinate axis by $2e^2/h$. The temperatures corresponding to the averaging of conductance over the particle energies and magnetic fields *B* are indicated near the lines ($T = 0$ for case *2*).

degenerate, as in an ideal triangle [13]. The doublet splitting of the oscillations can be caused by the asymmetry of the system.

In our measurements, the temperature dependence of the oscillation amplitude is not too strong in the range 0.04–1.5 K (Figs. 1a, 1b), due to the small size of the dot (100 nm). Therefore, we can conclude that the energy levels manifested in the oscillations are spaced by more than 0.1 meV. This conclusion is consistent with the calculation of the number of electrons (20–25) [8] and the potential-well depth (5–6 meV) in the quantum dot for $V_g = 0$.

According to both the indirect experimental data published in [14] and calculations of magnetotransport [15] in small ring interferometers, the presence of even a weak magnetic field ($B = 0.5$ T) both suppresses backscattering arising in the contacts between the entrance channel with the ring and improves the quantization of conductance. In other words, the peaks of the resistance of structures in the absence of the magnetic field correspond to states with negative magnetoresistance in weak magnetic fields [15]. This fact is qualitatively consistent with our measurements (Figs. 1b, 1c). It is seen that the field $B = 0.4$ T suppresses oscillations in G and R_{1213}^{-1} for a lower conductance plateau of $2e^2/h$.

To corroborate the interference nature of the conductance oscillations, we simulate the electrostatics of the device and coherent single-particle magnetotransport. Figure 2 shows the results.

The effective potential in the 2D gas is calculated with the replacement of the random charge distribution in the delta-doping layers by a more uniform distribu-

tion. Moreover, the coordinate dependence of the etching depth within the etching region is disregarded. Antidots were treated as ideally circular; they had identical diameters, and cuts were represented by rectangles of identical width. Under these assumptions, the quantum dot is close in shape to the regular triangle whose vertices are connected by narrow contacts with the remaining 2D electron gas. The actual effective potential $U_{eff}(x, y)$ is not strictly symmetric due to technological tolerances, and asymmetry is primarily manifested in variations in the penetrability of three entrances to the dot [8, 16]. Therefore, to simulate the difference between nominally identical devices, the distances between the centers of antidots, as well as the total depth of etching, were slightly varied (within 10 nm). The electron penetrability of the dot in the absence of the magnetic field was calculated by the S-matrix method [6, 9, 15, 17]. Conductance was determined by the multichannel Landauer formula. The magnetic-field effect on the transmission of an electron was taken into account by recursive Green's functions [18]. For simplicity, the shape of the effective electrostatic potential was assumed to be independent of the incident-particle energy E_F.

According to the transport calculations, the model of the triangular quantum dot under investigation provides for deep dips in conductance against the plateau background close to $2e^2/h$. Knowing the $E_F - U_{eff}(x, y)$ value, we found that the characteristic distance between dips in conductance, ΔE_F, corresponds to a change in the number of electrons in the quantum dot by about ten. Thus, the distance between dips of conductance that is measured using the value obtained for C_g agrees with the transport-theory value. As a whole, the pattern of the oscillations is similar to that obtained in measurements (Fig. 1). The difference in the oscillation forms for two different dot states is qualitatively reproduced. For case *2*, where the dot is less open and symmetric, the doublet splitting of the conductance peaks at zero temperature in the absence of the magnetic field is pronounced. Moreover, the splitting value corresponds to a change in the number of electrons in the dot by two or three; i.e., it is scattering on a pair of levels between which other quasidiscrete states are absent.

The calculated response of the conductance of the three-terminal dots to both an increase in temperature and the appearance of the magnetic field is qualitatively similar to the measured response of R_{1213}^{-1} and G to changes in T and B. However, for $B = 0.4$ T, narrow dips remain in the $2e^2/h$-conductance line calculated for state *2*. These dips are absent in the measurements. For this state and for $B = 0$, the dips are more pronounced than those observed in the measurements. However, they become noticeably less pronounced when one antidot moves from two others by only 10 nm (state *1*). Therefore, real differences in the widths of entrances to the dot can be responsible for the decrease in the ampli-

tude of interference oscillations. It should be noted that the magnetic field strongly affects the mode composition of the ballistic transport. In particular, the basic contribution to the penetrability of the quantum dot for $B = 0.4$ T comes from three higher modes (10, 11, 12) rather than from the first modes of the wide entry channel as for $B = 0$. With a further increase in B, the contribution from these modes decreases, and lower modes dominate again. As a whole, the calculations of the magnetotransport properties of the three-terminal dot under investigation corroborate the idea that single-particle interference and quantum-size effects play the decisive role in the formation of the observed oscillations.

Figure 3 shows the microscopic interference pattern for the most interesting features of conductance.

Wave functions were calculated by the recursive Green's functions method [19]. Figures 3a and 3b correspond to neighboring states of high reflection and transmission in the absence of a magnetic field (marked by the asterisk in Fig. 2a). It is assumed that electrons are incident from the left and they belong to the first mode of the wide entrance channel. For the case of strong reflection, the wave function is a standing wave that arises between the antidot and reservoir. The high peaks of the probability density are in the entrance constriction, and a ballistic electron does not fall to other constrictions (Fig. 3a). On the contrary, in the complete-penetrability state of the triangular dot, a traveling wave exists in all constrictions, and the high peaks of the probability density are attributed to the triangular quantum dot (Fig. 3b). Interference patterns inside the quantum dot are qualitatively different for these two states. Therefore, the corresponding E_F values are close to different quasidiscrete levels.

Figure 3c shows the probability-density plot corresponding to a state with $E_F = 1.7$ meV in a weak magnetic field of $B = 0.4$ T, when the penetrability of the triangular dot increases to 0.8. The result of scattering is presented for the 11th mode of the wide entrance channel, which makes the largest contribution to the dot penetrability. Comparison between Figs. 3a and 3c shows that the suppression of backscattering is caused by the appearance of significant asymmetry in the interference pattern for $B = 0.4$ T. This magnetic field begins to press the electron flux to the upper antidot, and this flux hence passes through the quantum dot to the upper dot contact in Fig. 3c. This behavior is similar to that for a small ring interferometer [14, 15].

Thus, various experimental facts (conductance oscillations, as well as strong backscattering and its suppression by the magnetic field) are consistent with the model of coherent transport in the small quantum dot. We have studied a device that is a quantum-scattering-based transistor triggering under the addition of several electrons to the dot. Moreover, the above results demonstrate that it is important to take into account quantum scattering at the current splitting points exist-
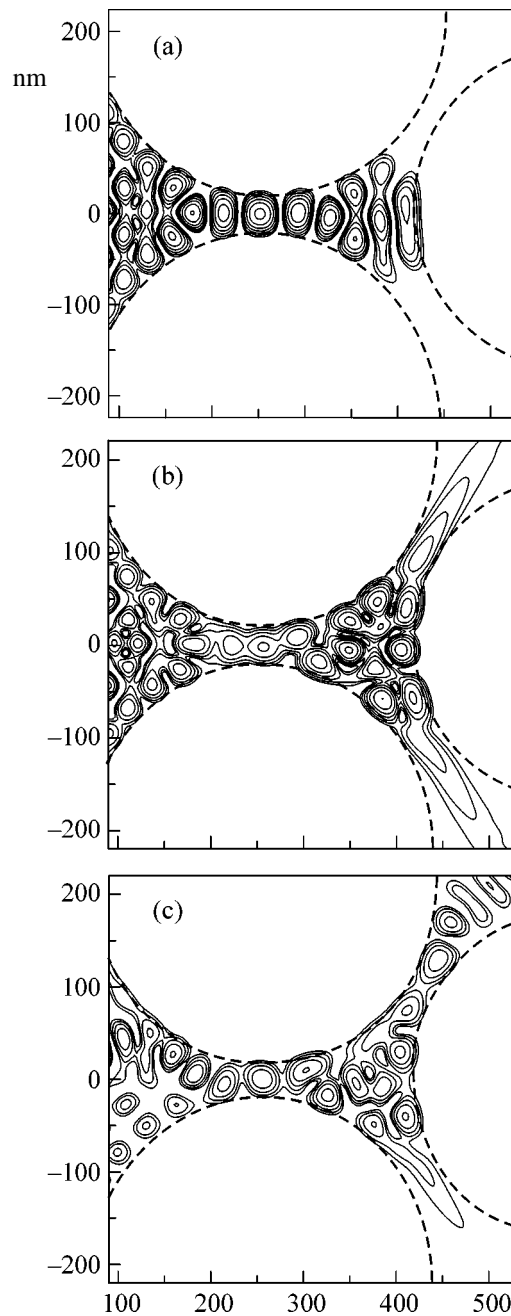

Fig. 3. Probability density distribution in the waves incident on the triangular dot from the left for cases marked by the asterisk in Fig. 2. Contours are drawn through equal values in the logarithmic scale. The dashed lines correspond to the condition $E_F = U_{eff}(x, y)$. The quantum-dot state with (a) $G = 0.06$, (b) 2, and (c) 1.6 e^2/h for $E_F =$ (a) 1.7 ($B = 0$), (b) 2.7 ($B = 0$), and (c) 1.7 meV ($B = 0.4$ T) are shown.

ing in ring interferometers [6, 9, 14] and Y transitions [20, 21].

REFERENCES

1. L. D. Landau and E. M. Lifshitz, *Course of Theoretical Physics*, Vol. 3: *Quantum Mechanics: Non-Relativistic Theory*, 3rd ed. (Nauka, Moscow, 1974; Pergamon, New York, 1977).

2. V. L. Al'perovich, V. A. Tkachenko, O. A. Tkachenko, *et al.*, Pis'ma Zh. Éksp. Teor. Fiz. **70**, 112 (1999) [JETP Lett. **70**, 117 (1999)].

3. M. Büttiker, Y. Imry, and R. Landauer, Phys. Lett. A **96**, 365 (1983); Y. Gefen, Y. Imry, and M. Ya. Azbel, Phys. Rev. Lett. **52**, 129 (1984).

4. Z. D. Kvon, L. V. Litvin, V. A. Tkachenko, and A. L. Aseev, Usp. Fiz. Nauk **169**, 471 (1999) [Phys. Usp. **42**, 402 (1999)].

5. C. M. Marcus, R. M. Westervelt, P. F. Hopkins, and A. C. Gossard, Phys. Rev. B **48**, 2460 (1993).

6. O. A. Tkachenko, V. A. Tkachenko, D. G. Baksheev, *et al.*, Pis'ma Zh. Éksp. Teor. Fiz. **71**, 366 (2000) [JETP Lett. **71**, 255 (2000)].

7. O. Estibals, Z. D. Kvon, J. C. Portal, *et al.*, Physica E (Amsterdam) **13**, 1043 (2002).

8. V. A. Tkachenko, Z. D. Kvon, O. A. Tkachenko, *et al.*, Pis'ma Zh. Éksp. Teor. Fiz. **76**, 850 (2002) [JETP Lett. **76**, 720 (2002)].

9. V. A. Tkachenko, A. A. Bykov, D. G. Baksheev, *et al.*, Zh. Éksp. Teor. Fiz. **124**, 351 (2003) [JETP **97**, 317 (2003)].

10. J. Gores, D. Goldhaber-Gordon, S. Heemeyer, *et al.*, Phys. Rev. B **62**, 2188 (2000).

11. O. A. Tkachenko, V. A. Tkachenko, D. G. Baksheyev, *et al.*, J. Phys.: Condens. Matter **13**, 9515 (2001).

12. J. P. Bird, R. Akis, D. K. Ferry, *et al.*, Phys. Rev. Lett. **82**, 4691 (1999).

13. I. V. Zozulenko, A. S. Shachrajda, C. Gould, *et al.*, Phys. Rev. Lett. **83**, 1838 (1999).

14. A. A. Bykov, D. V. Nomokonov, A. K. Bakarov, *et al.*, Pis'ma Zh. Éksp. Teor. Fiz. **78**, 36 (2003) [JETP Lett. **78**, 30 (2003)].

15. O. A. Tkachenko, V. A. Tkachenko, D. G. Baksheev, *et al.*, Pis'ma Zh. Éksp. Teor. Fiz. **79**, 351 (2004) [JETP Lett. **79**, 293 (2004)].

16. V. A. Tkachenko, Z. D. Kvon, D. V. Shcheglov, *et al.*, Pis'ma Zh. Éksp. Teor. Fiz. **79**, 168 (2004) [JETP Lett. **79**, 136 (2004)].

17. M. Cahay, M. McLennan, and S. Datta, Phys. Rev. B **37**, 10125 (1988).

18. T. Ando, Phys. Rev. B **44**, 8017 (1991).

19. T. Usuki, M. Saito, M. Takatsu, *et al.*, Phys. Rev. B **52**, 8244 (1995).

20. I. Shorubalko, H. Q. Xu, I. Maksimov, *et al.*, Appl. Phys. Lett. **79**, 1384 (2001); S. Reitzenstein, L. Worschech, P. Hartmann, *et al.*, Phys. Rev. Lett. **89**, 226804 (2002).

21. D. Csontos and H. Q. Xu, J. Phys.: Condens. Matter **14**, 12513 (2002).

Translated by R. Tyapaev

Anomalous Slowing Down of the Longitudinal Spin Relaxation near the Antiferromagnetic Phase Transition in LaMnO₃ Manganite

V. A. Atsarkin*, V. V. Demidov*, and A. M. Balbashov**

* Institute of Radio Engineering and Electronics, Russian Academy of Sciences,
ul. Mokhovaya 18, Moscow, 125009 Russia
** Moscow Power Engineering Institute (Technical University),
ul. Krasnokazarmennaya 14, Moscow, 105835 Russia
Received October 6, 2004

It has been found that, instead of the expected critical acceleration of the longitudinal spin relaxation near the Néel temperature in stoichiometric LaMnO₃ samples, the relaxation is sharply retarded. This slowing down is similar to that observed earlier in doped manganites with ferromagnetic ordering. © 2004 MAIK "Nauka/Interperiodica".

PACS numbers: 75.40.–s; 75.47.–m; 76.30.–v

The widespread interest in rare-earth manganites is caused by their unusual magnetic and transport properties (for instance, the collosal magnetoresistance) and their rich phase diagram that includes metal–insulator transitions and various spin-, orbital-, and charge-ordering types (see, e.g., reviews [1–3]). The physical nature of these properties is as yet far from fully understood. In particular, a phase-transition mechanism in manganites and, specifically, the possible role of microscopic phase separation accompanied by the formation of metallic ferromagnetic droplets (ferrons) is still the subject of acute controversy [2, 4]. Important information on the magnetic properties and spin dynamics at the microscopic level can be provided by the study of electron paramagnetic resonance (EPR) spectra (see, e.g., [5–10]). In addition to the data on the transverse spin relaxation time T_2, which is extracted from the EPR line width, measurements of the longitudinal spin relaxation time T_1, whose inverse is known [11] to be proportional to the spectral density $J(\omega_0)$ of local-field fluctuations at the EPR frequency ω_0, may be quite informative. Measurements of the time T_1 in manganites have become possible due to the use of the modulation technique with detection of the longitudinal spin-magnetization component; this technique was proposed as early as the 1960s [12] and has recently been modified [13, 14] for measurements of very fast relaxation processes with rates $T_1^{-1} \sim 10^{-9}$–10^{-10} s.

This technique was used to measure the temperature dependence of T_1 in the paramagnetic phase of doped manganites with the compositions La₁₋ₓCaₓMnO₃ ($0.1 \leq x \leq 0.33$) [15–17] and La₂₋₂ₓSr₁₊₂ₓMn₂O₇ ($x = 0.4$) [18]. These measurements showed that, instead of the theoretically predicted [19] critical acceleration of relaxation, it was retarded as the ferromagnetic-transition temperature (T_C) was approached. The absence of critical acceleration near T_C was also established for some ferrites [20, 21]. In an effort to physically explain this phenomenon, the possible role of the polarization of superparamagnetic clusters or ferromagnetic droplets in the presence of a static magnetic field $B_0 \sim 3$ kG, which is necessary for the observation of EPR, was pointed out in [15–18] (the possibility of suppressing critical relaxation acceleration by an external magnetic field was theoretically analyzed in [22]). However, an ultimate interpretation of the indicated anomaly is presently lacking. It is worth noting that, in all cases described so far, critical relaxation acceleration was absent in materials with ferromagnetic ordering.

The purpose of this work was to study the temperature dependence of T_1 near the phase transition in the "parent" (undoped) LaMnO₃ manganite that is known to undergo a transition from the paramagnetic to the antiferromagnetic state upon cooling [1–3]. Therefore, it had to reveal whether the anomalous slowing down of the longitudinal spin relaxation is an exceptional property of the ferromagnetic phase transition or whether it is typical of all manganites, including antiferromagnetic ones.

Single crystals of LaMnO₃ were grown by zone melting; the details of this procedure are described in [23]. The single-phase character of the synthesized crystals was monitored by x-ray structural analysis. However, the accuracy of this method is insufficient for the detection of small (about one percent) deviations from stoichiometry. As is known [24], such deviations are described by the formula (LaMn)₁₋δO₃ and give
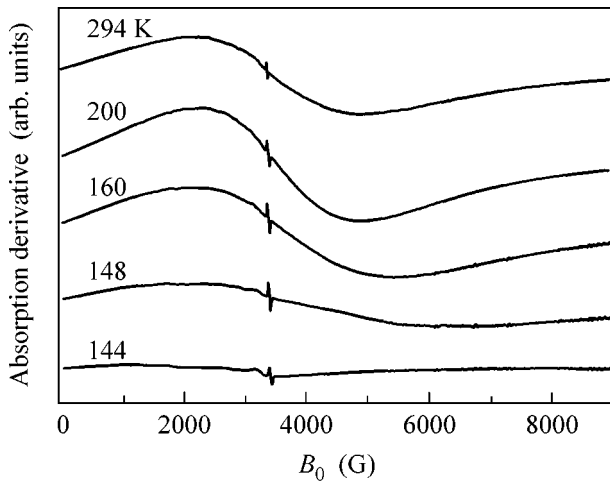
Fig. 1. The EPR spectra of $LaMnO_3$ at various temperatures. The narrow line near 3400 G is the reference.
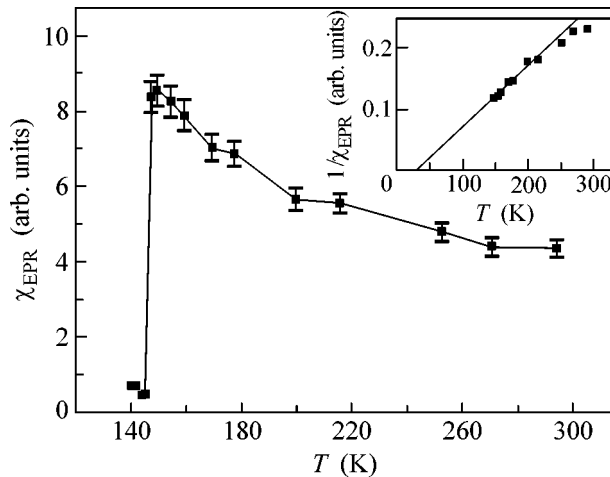

Fig. 2. Temperature dependence of the magnetic susceptibility, as obtained by the double integration of the EPR spectra (the broken line passes through the experimental points). Inset: the temperature dependence of the inverse susceptibility above T_N; the straight line corresponds to the Curie–Weiss law.

two samples in which these effects were absent. All results presented below were obtained for these samples, whose spectra and relaxation rates proved to be identical.

Measurements were made in a wavelength range of 3.2 cm (*X* band). The EPR spectra were recorded on a standard ER-200 (Bruker) spectrometer. The longitudinal relaxation time was measured in the same frequency range on an original setup described in [13, 14]. The microwave power modulation and the lock-in detection of the longitudinal magnetization component were performed at a frequency of 1.6 MHz. The "amplitude" version of the method was employed, in which the in-phase component of the longitudinal response caused by weak EPR saturation was compared with the unsaturated EPR absorption signal recorded under the same conditions. The Y_2BaCuO_5 compound was used as a reference, for which the time $T_1 = 10^{-9}$ s is independent of temperature in the range 140–300 K studied in this work [14]. Because of the design features of the coaxial microwave cavity used (see [14]), the $LaMnO_3$ single crystals were powdered and the powder was mixed with an Y_2BaCuO_5 powder, poured over with paraffin, and uniformly plunged into a toroidal container.

The typical EPR spectra recorded at different temperatures are shown in Fig. 1. At $T > 145$ K, the spectrum consists of a single line of an approximately Lorentzian shape with a width that has a shallow minimum near 180 K and increases strongly upon further cooling. Near 145 K, the EPR line is abruptly weakened (almost disappears), which indicates the antiferromagnetic phase transition. All these features are in agreement with the literature data [8, 26].

Figure 2 shows the temperature dependence of the integrated EPR absorption intensity, i.e., magnetic susceptibility χ_{EPR} obtained by the double integration of the spectra shown in Fig. 1. The approximation of the $1/\chi_{EPR}(T)$ dependence by the Curie–Weiss law with the parameter $\theta \cong 30$ K is demonstrated in the inset. The ferromagnetic sign of the Curie–Weiss temperature does not contradict the antiferromagnetic ordering with the alternation of oppositely polarized ferromagnetic planes and reflects the fact that the sum of the ferromagnetic exchange integrals $4J_{ac}$ for four neighbors in the crystallographic *ac* plane exceeds the corresponding sum $2J_b$ of the antiferromagnetic integrals for two neighbors in adjacent planes [26].

The temperature dependences of the longitudinal and transverse relaxation times are shown in Fig. 3. The corresponding values of T_2^* were determined from the EPR line width according to the formula

$$(T_2^*)^{-1} = (\sqrt{3}/2)\Delta B_{pp},$$

rise to the appearance of Mn^{4+} ions (holes) that favor the additional exchange interaction of the ferromagnetic sign. Experiments suggest (see, e.g., [25]) that the narrowing of a broad Lorentzian EPR line, typical of $LaMnO_3$, or the appearance of a narrower and rapidly growing component against its background upon cooling down to T_N can serve as a sensitive indicator of the aforementioned deviations. For this reason, among numerous single crystals with the nominal formula $LaMnO_3$ that were grown under various technological conditions (with varied oxygen content in the growth medium, temperature variation rate, etc.), we selected

where ΔB_{pp} is the EPR line width between the derivative peaks (the asterisk on T_2 indicates the possible contribution of inhomogeneous broadening).

One can see in Fig. 3 that T_1 and T_2^* approximately coincide at sufficiently high temperatures, which is natural in the situation of strong exchange narrowing (fast-motion limit [11]). However, as T_N is approached, the time T_1 starts to increase, whereas T_2^* shortens. Fitting the temperature dependence of longitudinal relaxation to the law

$$T_1 \propto (T/T_N - 1)^{-\alpha} \qquad (1)$$

yields the critical exponent $\alpha = 0.5$ (solid line in Fig. 3).

Thus, the behavior of longitudinal relaxation near the antiferromagnetic phase transition in $LaMnO_3$ proved to be qualitatively the same as in doped manganites undergoing ferromagnetic ordering [15–18], including the critical-exponent value [15].

Attempts to explain this unexpected result within the framework of the hypotheses used in the ferromagnetic case require substantial improvements. One is forced to assume that ferromagnetic (or, at least, ferromagnetically correlated) clusters arise in pure $LaMnO_3$, whose lattice does not contain Mn^{4+} ions (holes). This seems to be possible under the assumption that ferromagnetic correlations in the ac planes arise upon cooling somewhat earlier than antiferromagnetic correlations between the neighboring planes. Note that the main contribution to the longitudinal response measured by the above method comes from those spins that are saturated more easily, i.e., which have the longest time T_1. It is conceivable that such spins enter into the ferromagnetically correlated regions in the ac planes that arise and expand immediately before antiferromagnetic ordering between the neighboring planes. As known, the competition between ferro- and antiferromagnetic orderings is typical of manganites and is manifested, in particular, in the suppression of antiferromagnetism even in a parent material doped with isomorphic diamagnetic impurities (e.g., Ga) [27]. Note that the possible mechanism for the disappearance of the critical relaxation acceleration in systems with competing ferro- and antiferromagnetic interactions was considered theoretically in [28, 29]. However, one cannot exclude the possibility that the critical relaxation acceleration nevertheless occurs in the immediate vicinity of T_N, but the longitudinal response cannot be detected and T_1 cannot be measured because of the sharp broadening and almost complete disappearance of the EPR line.

Thus, undoped $LaMnO_3$ manganite has been taken as an example to demonstrate the absence of the critical acceleration of the longitudinal spin relaxation in systems with the antiferromagnetic phase transition. The observed increase in the time T_1 is due to the formation of the ferromagnetically correlated regions that pre-
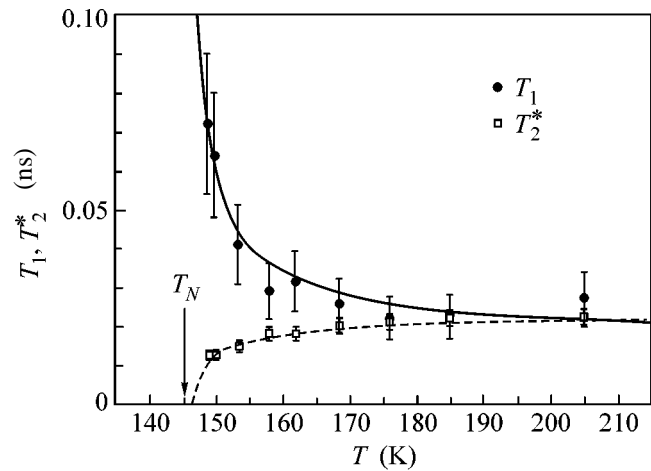

Fig. 3. Temperature dependences of the longitudinal (T_1) and transverse (T_2^*) relaxation times in the paramagnetic phase of $LaMnO_3$. The solid line is the fit to formula (1) (see text). The dashed curve passes through the experimental points for clarity.

cedes antiferromagnetic ordering. To get deeper insight into the nature of the observed effect, further experimental and theoretical studies are required.

REFERENCES

1. J. M. D. Coey, M. Viret, and S. Von Molnar, Adv. Phys. **48**, 167 (1999).
2. E. L. Nagaev, Phys. Rep. **346**, 387 (2001).
3. E. Dagotto, J. Hotta, and A. Moreo, Phys. Rep. **344**, 1 (2001).
4. M. Yu. Kagan and K. I. Kugel', Usp. Fiz. Nauk **171**, 577 (2001) [Phys. Usp. **44**, 553 (2001)].
5. A. Shengelaya, G. Zhao, H. Keller, and R. A. Muller, Phys. Rev. Lett. **77**, 5296 (1996).
6. M. T. Causa, M. Tovar, A. Caneiro, et al., Phys. Rev. B **58**, 3233 (1998).
7. J. Deisenhofer, B. I. Kochelaev, E. Shilova, et al., Phys. Rev. B **68**, 214427 (2003).
8. D. L. Huber, G. Alejandro, A. Caneiro, et al., Phys. Rev. B **60**, 12155 (1999).
9. A. I. Shames, E. Rozenberg, G. Gorodetsky, and Ya. M. Mukovski, Phys. Rev. B **68**, 174402 (2003).
10. G. Alejandro, M. C. G. Passeggi, D. Vega, et al., Phys. Rev. B **68**, 214429 (2003).
11. C. P. Slichter, *Principles of Magnetic Resonance,* 3rd ed. (Springer, Berlin, 1990; Mir, Moscow, 1981), Chap. 5.
12. J. Pescia, Ann. Phys. (Paris) **10**, 389 (1965).
13. V. A. Atsarkin, V. V. Demidov, and G. A. Vasneva, Phys. Rev. B **52**, 1290 (1995).

14. V. A. Atsarkin, G. A. Vasneva, and V. V. Demidov, Zh. Éksp. Teor. Fiz. **108**, 927 (1995) [JETP **81**, 509 (1995)].

15. V. A. Atsarkin, V. V. Demidov, G. A. Vasneva, and K. Conder, Phys. Rev. B **63**, 092405 (2001).

16. V. A. Atsarkin, V. V. Demidov, G. A. Vasneva, and D. G. Gotovtsev, Appl. Magn. Reson. **21**, 147 (2001).

17. V. A. Atsarkin, V. V. Demidov, F. Simon, *et al.*, J. Magn. Magn. Mater. **258–259**, 256 (2003).

18. F. Simon, V. A. Atsarkin, V. V. Demidov, *et al.*, Phys. Rev. B **67**, 224433 (2003).

19. D. L. Huber, J. Phys. Chem. Solids **32**, 2145 (1971); Phys. Rev. B **6**, 3180 (1972).

20. V. N. Berzhanskii and V. I. Ivanov, Phys. Status Solidi B **151**, 259 (1989).

21. I. Laulicht, J. T. Suss, and J. Barak, J. Appl. Phys. **70**, 2251 (1991).

22. A. V. Lazuta, S. V. Maleev, and B. P. Toperverg, Zh. Éksp. Teor. Fiz. **81**, 2095 (1981) [Sov. Phys. JETP **54**, 1113 (1981)].

23. A. A. Mukhin, V. Yu. Ivanov, V. D. Travkin, *et al.*, Pis'ma Zh. Éksp. Teor. Fiz. **68**, 331 (1998) [JETP Lett. **68**, 356 (1998)].

24. Q. Huang, A. Santoro, J. W. Lynn, *et al.*, Phys. Rev. B **55**, 14987 (1997).

25. S. B. Oseroff, M. Torikachvili, J. Singley, *et al.*, Phys. Rev. B **53**, 6521 (1996).

26. M. T. Causa, G. Alejandro, R. Zysler, *et al.*, J. Magn. Magn. Mater. **196–197**, 506 (1999).

27. J. Blasco, J. Garcia, J. Campo, *et al.*, Phys. Rev. B **66**, 174431 (2002).

28. S. V. Maleev, Pis'ma Zh. Éksp. Teor. Fiz. **26**, 523 (1977) [JETP Lett. **26**, 383 (1977)].

29. V. N. Berzhanskii and V. I. Ivanov, Phys. Status Solidi B **151**, 259 (1989).

Translated by V. Sakun

Ultrasonic Study of the Phase Diagram of Methanol

E. L. Gromnitskaya, O. V. Stal'gorova, O. F. Yagafarov, V. V. Brazhkin, A. G. Lyapin, and S. V. Popova

Institute of High-Pressure Physics, Russian Academy of Sciences, Troitsk, Moscow region, 142190 Russia
Received October 8, 2004

The phase diagram of methanol is studied by an ultrasonic technique over the temperature range 90–290 K at pressures up to 1.2 GPa. The pressure and temperature dependence of the velocity of longitudinal ultrasonic waves and the density of crystalline and liquid phases has been determined. Weak anomalies in the velocity of ultrasound in the liquid phase of methanol and the corresponding anomalous additional compression of the liquid at 230–250 K and 0.2–0.6 GPa have been found, and they are likely attributable to structural changes in the liquid phase. © *2004 MAIK "Nauka/Interperiodica".*

PACS numbers: 62.20.Dc; 62.50.+p; 64.70.Kb

1. Methanol is a simple model substance that can be used to study the nature of intermolecular interactions in systems with hydrogen bonds. Unlike ice and water, which are substances with strong tetrahedrally ordered hydrogen bonds under normal conditions, methanol (as well as ethanol) is considered to be a classical model substance with medium-strength hydrogen bonds and a chain structure in both crystalline and liquid states [1–5]. Alcohols have been studied to a much lesser extent than water. Experimental data on the *p–T* phase diagrams and physical properties of alcohols are scanty. Moreover, data on the structures of both crystalline and liquid phases are contradictory in many cases [1–6].

Methanol exhibits a complicated behavior under changes in pressure (*p*) and temperature (*T*). The weakening of hydrogen bonds in liquid methanol heated to high temperatures was unambiguously established. At the same time, there are various opinions regarding the effect of pressure on the strength of hydrogen bonds in methanol [5, 7–9]. Thus, for example, Bai and Yonker [5] pointed to an increase in the length of hydrogen-bonded linear chains in liquid methanol with pressure. However, Jorgensen and Ibrahim [7] found that a volume decrease occurred due to a change in the distance between chains, whereas the chain length remained unchanged in this case. At the same time, Giguere and Pigeon-Gosselin [9] concluded that the structure of liquid methanol is a three-dimensional network rather than chains and that the effect of pressure on liquid methanol can lead to structural disordering.

At atmospheric pressure, as the temperature is decreased, methanol crystallizes to form a high-temperature β phase at *T* = 175 K. As the temperature is further decreased, a solid-phase transition from the β to α phase occurs at *T* = 157 K [10–14]. At low temperatures, the phase diagram of methanol was studied by differential thermal analysis over a narrow range of pressures (to 0.3 GPa at 77–293 K) [15]. In the case of

compression at room temperature, methanol crystallizes at *p* ≈ 3.5 GPa, but the structure of crystalline methanol at high pressures (*p* > 3 GPa) was determined ambiguously [1, 13, 16]. At a high loading rate, liquid methanol can be in an overcompressed state (that is, liquid below the melting temperature) and can undergo a glass transition at 5–10 GPa [1, 16, 18]. Relatively strong hydrogen bonds and a considerable structural difference between the liquid and solid phases of methanol are likely favorable for the glass transition in liquid methanol.

The physical properties of methanol, including its elastic characteristics, are not only of fundamental interest but also of paramount importance to experimental high-pressure physics. This is due to the fact that both neat methanol and a 4 : 1 methanol–ethanol mixture are frequently used as a truly hydrostatic medium up to *p* ~10 GPa [19]. The elastic properties of methanol under pressure (to 6.8 GPa) were studied previously only at room temperature using stimulated Brillouin scattering in diamond anvil cells [20]. To the best of our knowledge, studies on the elastic properties of crystalline methanol phases have not yet been performed.

The aim of this work was (i) to study the elastic properties of methanol at low temperatures and high pressures with the use of an ultrasonic technique in combination with direct volumetric measurements and (ii) to construct the phase diagram of methanol based on these measurements.

2. The measurements were performed with a low-temperature ultrasonic piezometer at pressures up to 1.2 GPa over the temperature range 90–290 K in accordance with the procedure described in [21]. After purification and drying, the test substance was placed in a cell made as a thin-walled Teflon beaker with a copper cap. The travel time of a longitudinal ultrasonic wave (to within 0.001 µs) was directly measured on an orig-
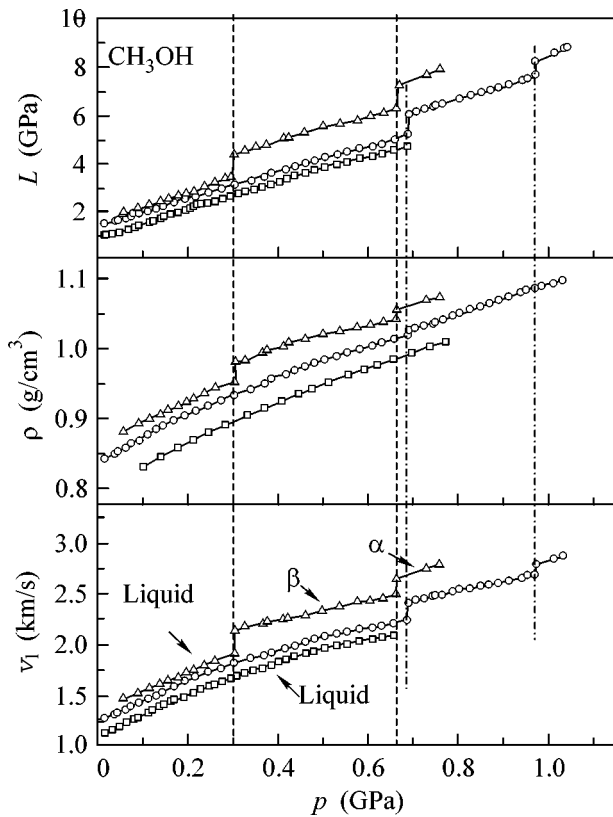
Fig. 1. Typical experimental pressure dependence of the velocity of the longitudinal ultrasonic wave v_l, the density ρ, and the longitudinal elastic modulus L in methanol compressed at temperatures ($\triangle$) 204, ($\circ$) 228, and ($\square$) 293 K. The vertical dashed lines correspond to the crystallization of the liquid into the β phase and to the β–α phase transition at $T = 204$ K. The dash–dotted lines mark the above phase transitions at $T = 228$ K.

inal Akustomer-1 system, which was developed at the Institute of High-Pressure Physics, Russian Academy of Sciences and which is based on MATEK instrumentation. Quartz plates with a carrier frequency of 5 MHz were used as piezoelectric transducers. In the experiments, changes in the ultrasonic signal paths were also measured to within 0.01 mm using angular-displacement indicators. The density of samples under pressure was determined from the change in their length.

Two series of experiments were performed to determine (i) the pressure dependence of the travel time of a longitudinal ultrasonic wave and the sample length at a constant temperature and (ii) the temperature dependence of the above characteristics under natural heating of a high-pressure chamber at a constant pressure (the heating rate was 1 K/min). As a result, the pressure and temperature dependence of the velocity of longitudinal ultrasonic waves $v_l(p, T)$ was found over a range from atmospheric pressure to 1.2 GPa at temperatures from 90 to 290 K. Anomalies in the changes in the above characteristics were localized as melting points or β–α phase-transition points in crystalline methanol. An

advantage of the ultrasonic technique is the capability of observing phase transitions accompanied by small volume changes and of almost continuously monitoring the parameters to be measured along with the simultaneous sufficiently accurate determination of phase-transition temperatures and pressures. More than 30 experiments were performed, which enabled us to decrease noticeably the statistical error.

Figure 1 demonstrates the isothermal pressure dependence of the velocity of the longitudinal ultrasonic wave v_l, the density of methanol ρ, and the modulus of elongation $L = \rho v_l^2$ for crystalline and liquid phases. These curves were obtained in the process of compression of initially liquid methanol. The absence of direct structure measurements in this study was compensated by published data on structure and Raman studies [1, 13, 15, 16]. In comparison with our measurements of the travel time of an ultrasonic signal and the density, this enabled us to reliably identify the phase transitions observed.

The shear modulus of the liquid phase is equal to zero, $G = 0$, and the longitudinal elastic modulus coincides with the bulk modulus, $L = B$, in accordance with the well-known equation for the velocity of longitudinal acoustic waves in isotropic media: $\rho v_l^2 = B + (4/3)G$. In Fig. 1, the vertical dashed lines indicate pressures corresponding to the crystallization of the liquid into the β phase and to the β–α phase transition at 204 K. The crystallization of the liquid phase at $T = 204$ K occurs with a density change of ≈ 0.030 g/cm^3 ($\approx 3.2\%$), a change in the velocity of longitudinal ultrasonic waves by ≈ 0.240 km/s ($\approx 12.6\%$), and an increase in the longitudinal elastic modulus by ≈ 0.9 GPa ($\approx 26\%$). As the temperature was increased (Fig. 1, curves for $T = 235$ K), the points of both phase transitions were naturally shifted toward higher pressures; the phase transitions occurred with smaller changes in the measured characteristics; the density (volume) changes became very small, and the β–α phase transition was reliably detected only by changes in the longitudinal velocity of ultrasound and the longitudinal elastic modulus. Note that all of the above characteristics in the α phase increased with pressure more rapidly than those in the β phase. Thus, for example, at $T = 204$ K (Fig. 1), the pressure derivatives of the longitudinal elastic modulus in the α and β phases are ≈ 5.4 and ≈ 7.5, respectively. Note that the ultrasound velocities, densities, and bulk compression moduli measured for liquid methanol at room temperature in this work are consistent with published data [6, 20].

Figure 2 demonstrates the isobaric temperature dependence of the same parameters as in Fig. 1 obtained by heating crystalline methanol at various fixed pressures. As an example, we consider the experimental function $v_l(T)$ at $p = 0.35$ GPa. A weak change in the longitudinal ultrasound velocity at $110 < T < 180$ K obviously corresponds to the α phase of metha-

nol. As the temperature further increases from 180 to 185 K, the anomalies of the characteristics correspond to a transition to the crystalline β phase, which occurs in a narrow temperature range from 185 to 200 K. The next anomaly is observed at $200 < T < 213$ K and obviously corresponds to the melting of methanol. Note that, as the heating pressure is increased, the total volume change in the α–β and β–liquid phase transitions decreases. Even at $p = 0.6$ GPa, the densities of the α and β phases of methanol are very close, and the temperature dependence of the density does not enable us to detect a phase transition. However, the temperature dependence of the velocity of longitudinal ultrasonic waves reveals the α–β phase transition and demonstrates the existence of the β phase at these pressures. The phase transition from the α to the β phase is accompanied by a dramatic decrease in the longitudinal modulus of methanol at an almost unchanged density, which is indicative of a total decrease in bonding forces in the crystal lattice of the β phase.

3. The results of isobaric and isothermal experiments allowed us to extend and refine considerably the p–T phase diagram of methanol, which is shown in Fig. 3 in comparison with the previously known diagram [22]. Note that the resulting experimental phase diagram of methanol is consistent with published data [1, 15, 17, 19], although it is much more complete. Our measurements demonstrated that the region of the existence of the β phase of methanol is narrowed with pressure. However, the α–β phase transition and the melting of the β phase can be distinguished at least to 1.2 GPa.

The flattening of the melting curve of methanol at $p > 0.75$ GPa should be noted. In accordance with the Clausius–Clapeyron equation, taking into account that the density of a liquid phase is lower than the density of the corresponding crystal near the melting curve, such a behavior can be attributed to a high compressibility of liquid methanol or to an additional structural compaction of the liquid phase of methanol (at $p \sim 0.6$–0.7 GPa near the melting curve) as a result of changing the short-range liquid structure.

Indeed, in the experiments on heating methanol at 0.1–0.4 GPa, weak anomalies in the ultrasound velocity and density in the liquid phase were observed over the temperature range 230–250 K. Figure 4 demonstrates, on an enlarged scale, the temperature dependence of the density and bulk compression modulus of liquid methanol at $p = 0.35$ GPa. Although they are small, the anomalies exhibit a stable character and repeatability, and their amplitude is higher than the error of relative measurements. The points corresponding to the observed anomalies are marked in the phase diagram of methanol (Fig. 3). They lie in a narrow region, which can be hypothetically considered to be a boundary between two structural types of liquid methanol with higher and lower molecular packing densities. Note that this apparent boundary is consistent with the onset
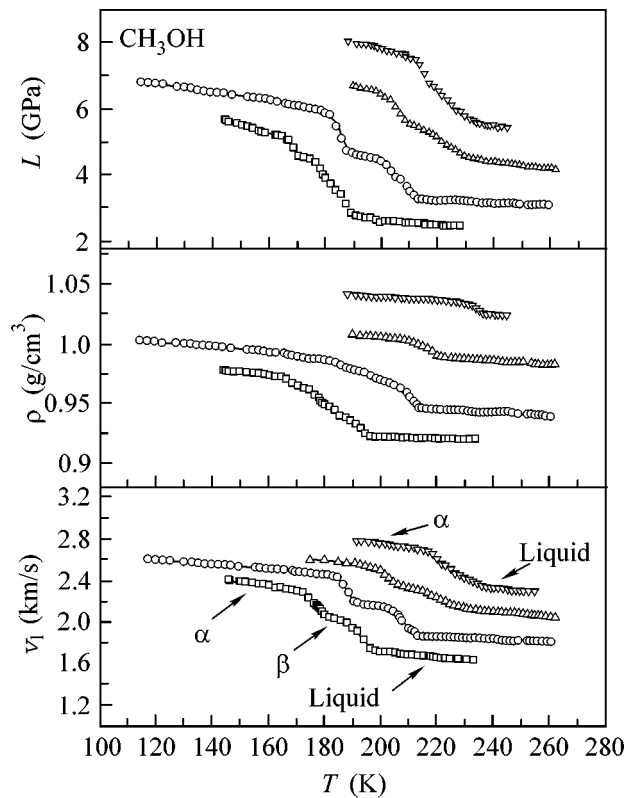

Fig. 2. Temperature dependence of the velocity of the longitudinal ultrasonic wave v_l, the density ρ, and the longitudinal elastic modulus L of methanol heated at fixed pressures (□) 0.22, (○) 0.35, (△) 0.6, and (▽) 0.85 GPa.

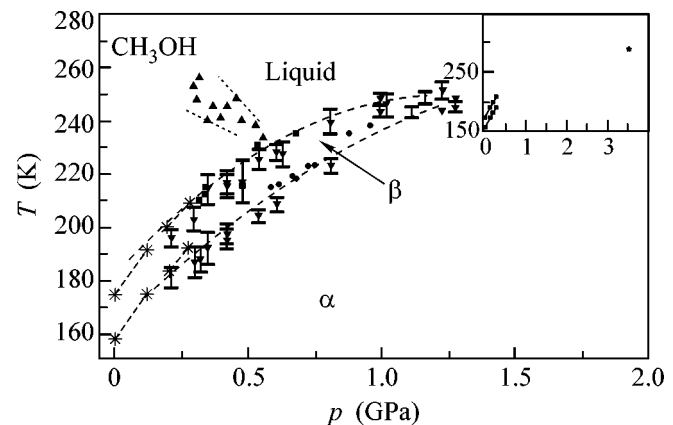**Fig. 3.** Phase diagram of methanol plotted using experimental data: (●) points corresponding to a transition from the liquid state to the β phase and the β–α phase transition as obtained in the methanol compression process; (▼) points corresponding to the α–β phase transition and the melting of methanol as obtained in the natural heating process; and (▲) points corresponding to anomalies in liquid methanol, which are grouped in the region marked with dotted lines. The dashed lines correspond to the interpolation of experimental phase-transition lines. The dashed lines at low pressures connect (∗) phase-transition points obtained by Wurflinger and Landau [15]. The inset shows phase-transition points in methanol under pressure, which correspond to the previously known phase diagram of methanol [22].
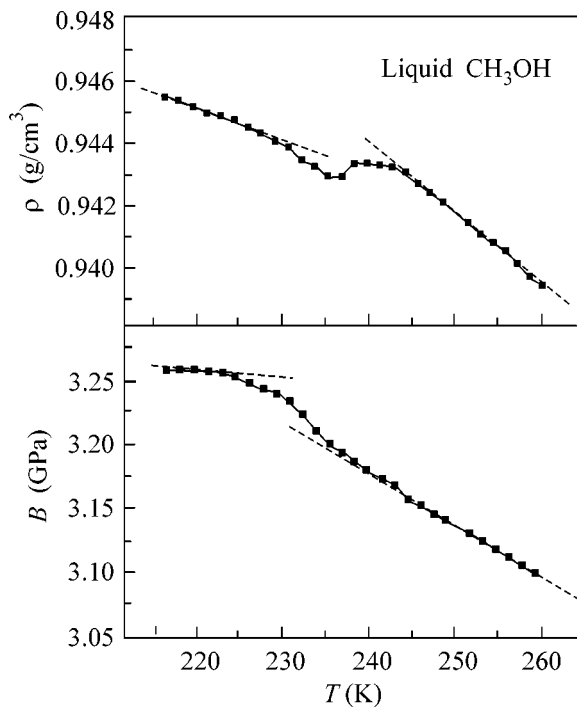
Fig. 4. Typical temperature dependence of the density and bulk modulus of liquid methanol measured at $p = 0.35$ GPa in the region of an anomaly that was regularly observed upon heating. The dashed lines are the approximations of the corresponding functions before and after the anomaly.
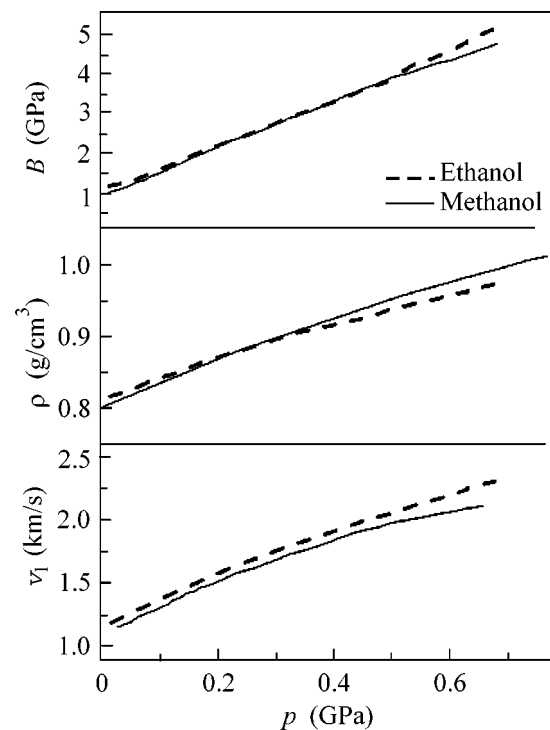

Fig. 5. Experimental pressure dependence of the velocity of the longitudinal ultrasonic wave v_l, the density ρ, and the bulk modulus B of (solid line) methanol and (dashed line) ethanol that are compressed at room temperature.

of flattening of the melting curve. This conclusion is tentative and requires further investigation, although the occurrence of anomalies in liquid methanol is a reliably established fact.

4. Thus, the p–T phase diagram of methanol over wide pressure and temperature ranges, as well as the elastic properties of crystalline and liquid phases, have been studied in this work using the ultrasonic technique.

It is of interest to compare the characteristics of liquid methanol and ethanol. Such a comparison is made in Fig. 5 for room temperature. Previous studies on the density and elastic properties of liquid methanol and ethanol under pressure [20] did not reveal differences in the behaviors of these substances under compression because of the low experimental accuracy. The results of a detailed study of ethanol under pressure will be published elsewhere. The pressure derivatives of the longitudinal elastic modulus of methanol phases are lower than those of ethanol. This is indicative of a weakening of the crystal lattice, and this weakening increases at $p > 0.5$ GPa. In this case, it is important that the density of liquid methanol increases more rapidly with pressure and becomes higher than the density of ethanol. As noted previously, the higher compressibility of methanol can be responsible for the flattening of the melting curve. Figure 5 provides support for this point of view.

As mentioned above, the melted methanol additionally experienced a sharp compaction at 0.2–0.6 GPa and 230–250 K (Fig. 4). This compaction is likely associated with structural changes in the liquid phase. It is of interest that a small increase in the density of the liquid is accompanied by a decrease in the bulk modulus (Fig. 4). Such an anomalous behavior was observed previously in hydrogen-bonded systems, in particular, in a phase transition between the crystalline H_2O phases ice 1h and ice III [23]. A more prominent example of such an anomaly was observed in D_2O ices [24]. In this case, the bulk modulus of the high-density amorphous (*hda*) ice, which is the densest phase, was noticeably lower than the corresponding bulk moduli of the low-density amorphous (*lda*) ice and the crystalline phases ice 1h and ice 1c.

Based on low-temperature Raman-scattering data, it is believed that a sharp transition from a quasi-chain structure of the liquid to a branched network structure involving several hydrogen bonds per molecule occurs in the process of compression of liquid methanol near the melting curve. The measurements of the density and elastic characteristics of crystalline and liquid alcohols over sufficiently wide ranges of pressures and temperatures will enable us to test various theoretical models and to significantly clarify the behavior of hydrogen bonds in simple alcohols under changes in thermodynamic parameters.

REFERENCES

1. J. F. Mammone, S. K. Sharma, and M. Nicol, J. Phys. Chem. **84**, 3130 (1980).

2. A. Arencibia, M. Taravillo, F. J. Perez, *et al.*, Phys. Rev. Lett. **89**, 195504 (2002).

3. E. M. Schulman, D. W. Dwyer, and D. C. Doetschman, J. Phys. Chem. **94**, 7308 (1990).

4. S. L. Wallen, B. J. Palmer, B. C. Garrett, and C. R. Yonker, J. Phys. Chem. **100**, 3959 (1996).

5. S. Bai and C. R. Yonker, J. Phys. Chem. **102**, 8641 (1998).

6. P. W. Bridgman, Proc. Am. Acad. Arts Sci. **74**, 399 (1942).

7. W. L. Jorgensen and M. Ibrahim, J. Am. Chem. Soc. **104**, 373 (1982).

8. T. Yamaguchi, K. Hidaka, and F. K. Soper, Mol. Phys. **96**, 1159 (1999).

9. P. A. Giguere and M. Pigeon-Gosselin, J. Solution Chem. **17**, 1007 (1998).

10. D. W. Davidson, Can. J. Chem. **34**, 124 (1956).

11. S. K. Garg and D. W. Davidson, J. Chem. Phys. **58**, 189 (1973).

12. H. G. Carlson and E. F. Westrum, Jr., J. Chem. Phys. **54**, 1464 (1971).

13. B. H. Torrie, O. S. Binbrek, M. Strauss, and I. P. Swainson, J. Solid State Chem. **166**, 415 (2002).

14. A. H. Narten and A. Habenschuss, J. Phys. Chem. **80**, 3387 (1984).

15. A. Wurflinger and R. Landau, J. Phys. Chem. Solids **38**, 811 (1977).

16. D. R. Allan, S. J. Clark, M. J. P. Brugmans, *et al.*, Phys. Rev. B **58**, R11809 (1998).

17. T. F. Sun, J. A. Schouten, N. J. Trappeniers, and S. N. Biswas, Phys. Chem. **92**, 652 (1988).

18. M. J. P. Brugmans and W. L. Vos, J. Phys. Chem. **103**, 2661 (1995).

19. G. J. Piermarini, S. Block, and J. D. Barnett, J. Appl. Phys. **44**, 5377 (1973).

20. J. M. Brown, L. J. Slutsky, K. A. Nelson, *et al.*, Science **241**, 65 (1988).

21. O. V. Stal'gorova, E. L. Gromnitskaya, D. R. Dmitriev, and F. F. Voronov, Prib. Tekh. Éksp. **39** (6), 115 (1996) [Instrum. Exp. Tech. **39**, 880 (1996)].

22. E. Yu. Tonkov, *High Pressure Phase Transformations, A Handbook* (Metallurgiya, Moscow, 1988; Gordon and Breach, Philadelphia, 1992), Vols. 1, 2.

23. G. H. Shaw, J. Chem. Phys. **84**, 5862 (1986).

24. E. L. Gromnitskaya, O. V. Stal'gorova, A. G. Lyapin, *et al.*, Pis'ma Zh. Éksp. Teor. Fiz. **78**, 960 (2003) [JETP Lett. **78**, 488 (2003)].

Translated by V. Makhlyarchuk

Stochastic Description of Phase Separation near the Spinodal Curve in Alloys[¶]

V. Yu. Dobretsov, I. R. Pankratov, and V. G. Vaks*

Russian Research Centre Kurchatov Institute, Moscow, 123182 Russia
*e-mail: vaks@mbslab.kiae.ru
Received October 4, 2004; in final form, October 11, 2004

The earlier-developed statistical methods for nonequilibrium alloys are applied to stochastically describe phase separation near the spinodal curve. An important parameter of the theory is the size of local equilibrium regions, which is estimated using simulations for the different values of this parameter. The simulations based on this approach reveal significant changes in the type of evolution from nucleation to spinodal decomposition under variation of concentration and temperature across the spinodal curve. The scale of these changes seems to be mainly determined by the difference of the properly defined supersaturation parameters. © *2004 MAIK "Nauka/Interperiodica"*.

PACS numbers: 05.70.Ln; 64.60.Qb

Studies of microstructural evolution in phase-separating alloys attract interest from both fundamental and applied points of view [1, 2]. Many detailed experimental [2–6] and theoretical [1] studies of these problems are available. However, up to now, the theoretical approaches seem to provide little information about the microscopical details of evolution [2]. There are two main kinetic forms of phase separation for an initially homogeneous system quenched into the two-phase equilibrium region: nucleation and spinodal decomposition. For definiteness, we consider the disordered binary alloy A_cB_{1-c}. There are two important curves in the concentration–temperature plane c, T: the two-phase equilibrium curve, or the binodal $T_b(c)$, and the stability limit of the uniform state, or the spinodal $T_s(c)$. The first curve is determined by the phase-equilibrium equations, and the second one is determined by the equation $(\partial^2 F/\partial c^2)_T = 0$, where $F = F(c, T)$ is the extrapolated or calculated expression for the free energy of the uniform alloy. According to classical ideas [7, 8], in the metastability region $T_s(c) < T < T_b(c)$, the homogeneous phase separation is realized via nucleation and growth (NG) of isolated precipitates of the new phase, while at $T < T_s(c)$ the main kinetic mechanism is spinodal decomposition (SD) via the development of unstable concentration waves with growing amplitudes. Taking into account the fluctuative effects (neglected in the classical theories) should result in some smearing of the borderline between these two evolution types in the c, T plane [1], though in the available experiments [3, 5] the transition region was found to be rather narrow. There are some detailed studies of NG at low supersaturation, i.e., near $T_b(c)$ [9, 10], as well as those for SD

at high supersaturation, i.e., well below $T_c(c)$ [11, 12]. However, there seems to be "no theoretical approach to describe the behavior in the transition region from SD to NG [1]." One can also mention the phenomenological treatments of this problem using the "stochastic-phase field equations," e.g., [13], but both the applicability region and the methods of calculating the fluctuative terms in these treatments seem to be unclear and arbitrary.

Recently, the microscopic generalized Gibbs distribution approach (GGDA) [14] has been suggested to study the diffusional kinetics of nonequilibrium alloys. Below, we use this approach to describe phase separation near the spinodal curve.

Let us first present the main equations of GGDA disregarding the fluctuative effects. Various distributions of atoms are described by the occupation numbers $\{n_i\}$, where n_i is 1 when the site i is occupied by atom A and 0 otherwise. GGDA is based on the master equation for the probability P to find the number set $\{n_i\} = \xi$,

$$dP(\xi)/dt = \sum_\eta [W(\xi, \eta)P(\eta) - W(\eta, \xi)P(\xi)], \quad (1)$$

where $W(\xi, \eta)$ is the $\eta \longrightarrow \xi$ transition probability per unit time, for which we use the conventional thermally activated atomic exchange model [14]. As discussed in detail in [14], for the usual conditions of phase transformations, the probability P in (1) can be written in the following "quasi-equilibrium" form:

$$P\{n_i\} = \exp\left[\beta\left(\Omega + \sum_i \lambda_i n_i - \sum_{i>j} v_{ij} n_i n_j\right)\right]. \quad (2)$$

[¶] This article was submitted by the authors in English.

Here, β is $1/T$; the parameters λ_i (being, generally, both time- and space-dependent) can be called the "site chemical potentials"; the quantities v_{ij} describe interatomic interaction supposed to be pairwise; and the constant $\Omega = \Omega\{\lambda_i\}$ is determined by the normalization.

Multiplying equation (1) by the operator n_i and summing over all configurational states, we obtain the "quasi-equilibrium" kinetic equation [14]:

$$dc_i/dt = \sum_j M_{ij}2\sinh[\beta(\lambda_j - \lambda_i)/2]. \tag{3}$$

Here, the mean site occupation c_i corresponds to the averaging of the operator n_i over distribution (2):

$$c_i = \langle n_i \rangle = \sum_{\{n_j\}} n_i P\{n_j\}, \tag{4}$$

and the "generalized mobility" M_{ij} is a similar average of some other function of occupation numbers. To explicitly find the functions $\lambda_i\{c_j\}$ and $M_{ij}\{c_k\}$ in Eqs. (3) and (4), we should use some approximate method of calculations. For example, in the simplest, "kinetic mean-field" approximation (KMFA), we obtain [14]

$$\lambda_i = T\ln(c_i/c_i') + \sum_j v_{ij}c_j, \tag{5}$$

$$M_{ij} = \gamma_{ij}[c_i c_i' c_j c_j' \exp(\beta u_i + \beta u_j)]^{1/2}, \tag{6}$$

where c_i' is $(1 - c_i)$, the factor γ_{ij} determines the probability of an intersite atomic exchange, and u_i is the "asymmetrical potential" supposed below to be zero.

For simplicity, we consider disordered cubic alloys at sufficiently high temperatures T not far from the critical temperature T_c, say, $T \gtrsim 0.9T_c$. Then, the space and time variations of the local concentration $c_i = c(\mathbf{R}_i, t)$ under phase separation are very smooth [8, 10], and Eqs. (3)–(6) can be rewritten in the continuous form [12]:

$$dc/dt = \text{div}[M(c)\beta\nabla\lambda(c)]; \tag{7}$$

$$\lambda(c) = T\ln(c/c') - 4T_c[c + (r_0^2/6)\nabla^2 c], \tag{8}$$

where $M(c)$ is $\gamma cc'$; γ is $\frac{1}{6}\sum_j \gamma_{ij}r_{ij}^2$ with $r_{ij} = |\mathbf{R}_i - \mathbf{R}_j|$; $T_c = (-\sum_j v_{ij}/4)$ is the critical temperature in the MFA used; and $r_0^2 = \sum_j v_{ij}r_{ij}^2 / \sum_j v_{ij}$ is the mean interaction radius squared. If, to calculate $\lambda_i\{c_j\}$ and $M_{ij}\{c_k\}$ in Eqs. (3) and (4), we use a more refined method than KMFA (e.g., kinetic cluster methods [14]), basic equation (7) retains its form but functions $\lambda(c)$ and $M(c)$ are

given by more complex expressions. This difference is unessential for what follows.

Let us look at a discrete description dividing the lattice into the cubic cells of size L (L-cells). To this end, we (i) sum Eq. (7) over all sites j within the cell centered at $\mathbf{R}_i$ ("cell i"), thus obtaining on the left-hand side $d\bar{N}_i/dt$, where $\bar{N}_i$ is $\sum_j c_j$; (ii) transform the right-hand side of (7) into surface integrals over six facets s of cell i; and (iii) integrate the result over a small time interval δt. Then, (7) takes the "finite difference" form:

$$\delta\bar{N}_i = \sum_{s=1}^{6} (L^2/v_a)\mathbf{n}_s\beta(M\nabla\lambda)_s\delta t. \tag{9}$$

Here, v_a is the volume per site; $\mathbf{n}_s$ is the unit vector normal to the facet s directed off the cell i; and the gradient term $\nabla\lambda$ is written as the appropriate finite difference. The mesh size L in (9) should be lower than the smallest inhomogeneity length, which, in our problem, is the interphase boundary width, while employing a larger L is convenient for computations. In our simulations, we used $L \gtrsim a$, where a is the face-centered cubic (FCC) lattice constant.

Let us now discuss the relation between the quantities c_i or $\bar{N}_i$ in (4) or (9) and the concentration distribution $c_{\text{obs}}(\mathbf{R}, t)$ observed experimentally. Note that the GGDA, being a statistical approach based on "ensemble averages" $c_i = \langle n_i \rangle$, is physically informative and complete only for a "macroscopically" nonequilibrium system ([7], Ch. 7) that can be divided into some locally equilibrated subsystems with the size l_{le} much exceeding the interatomic distance a. Within each subsystem, the site chemical potential λ_i in (2) is approximately constant, and its fluctuations have a relative scale $(a/l_{\text{le}})^{3/2} \ll 1$. Therefore, the summation over alloy states in Eq. (4) should include not all distributions $\{n_i\}$ but only those with the limited inhomogeneity lengths $l < l_{\text{le}}$, while the long-wave fluctuations with $l \gtrsim l_{\text{le}}$ remain to be fixed in the macroscopically nonequilibrium state under consideration. Therefore, the "diffusive" term on the right-hand side of Eqs. (7) or (9) corresponds just to a "coarse-grained" averaging in (4) performed at the fixed distribution of these long-wave fluctuations, and the terms allowing for their dynamics should also be considered to describe $c_{\text{obs}}(\mathbf{R}, t)$. These fluctuative terms were neglected in the previous GGDA-based treatments of phase transformations [14], as usually they have little effect on evolution. However, for the phase separation above and near the spinodal curve, the presence of such terms is crucial.

We describe these fluctuative terms using the stochastic Langevin-type approach. To this end, we proceed from the average $\bar{N}_i = \sum_j c_j$ in Eq. (9) to an "individual phase trajectory," that is, to the actual atom

number $N_i(t) = \sum_j n_j$ within each L cell. It differs from the average $\bar{N}_i(t)$ due to the fluctuations of the atomic transfer δN_{fs} across each facet s for the time interval δt. Therefore, instead of Eq. (9), we have

$$\delta N_i \equiv N_i(t + \delta t) - N_i(t) = \delta N_{di}\{c_j\} + \delta N_{fi}, \quad (10)$$

where the diffusive term δN_{di} is given by the right-hand side of Eq. (9) and the fluctuative term δN_{fi} is $\sum_s \delta N_{fs}$.

Following Langevin's idea [15], we treat each fluctuative transfer δN_{fs} as a random quantity with the Gaussian probability distribution $W(\delta N_{fs})$:

$$W(\delta N_{fs}) = A_s \exp(-\delta N_{fs}^2/2D_s), \quad (11)$$

where A_s is the normalization constant and the dispersion D_s is the same as that for the actual fluctuative transfer δN_{fs}. For example, for the nearest-neighbor atomic exchange model with γ_{ij} in (6) equal to γ_{nn}, the KMFA calculation of D_s yields

$$D_s = \langle \delta N_{fs}^2 \rangle = \gamma_{nn} \delta t N_b 2 c_s (1 - c_s), \quad (12)$$

where N_b is the total number of bonds crossed by each facet s. For the FCC lattice, N_b is $8L^2/a^2$, while the number of sites N_L within an L cell is $4L^3/a^3$.

Let us now discuss which quantities c_j should be used as the arguments for the local chemical potential $\lambda\{c_j\}$ and the mobility $M\{c_j\}$ in the "diffusive" term δN_{di} in (10). The most "natural" (but naive) prescription seems to be just to put $c_j = N_j/N_L$, that is, to treat the fluctuations of both the atom number N_i and the chemical potential $\lambda_i = \lambda_i\{c_j\}$ within each L cell on the same footing, which is declared, for example, in the "stochastic-phase field" treatments [13]. However, the numerical realization of this "direct" recipe for the reasonable L values mentioned above leads to physically unacceptable results, namely, to totally chaotic evolution with no hints of a tendency to thermodynamic equilibrium of any kind at any T and c.

If one arbitrarily decreases the fluctuation scale D_s in Eqs. (10)–(12) by one or two orders of magnitude, the evolution becomes more plausible. However, there seem to be no arguments for such a drastic reduction of fluctuations within this "direct" approach.

The physical origin of the failure of such a "direct" approach is the fundamental difference between the fluctuations of the "mechanistic" quantities N_i having a direct and measurable meaning and the fluctuations of the "thermodynamic" quantities λ_i describing the locally equilibrium subsystems. As mentioned, expression (9) for the diffusive term is obtained by the statistical averaging over all fluctuations of occupations $\{n_j\}$ except for those with the large wavelengths l exceeding the length l_{le} of a local equilibrium. Thus, it makes no

sense to include again the short-wave fluctuations in the diffusive term δN_{di} that has been already averaged over these fluctuations. The fluctuation of the parameter λ_i in (2) can have a physical meaning only if it takes an approximately identical value for the whole volume $V_{le} \sim l_{le}^3$, that is, if it has a wavelength $l \gtrsim l_{le} \gg L \sim a$. In other words, the total fluctuative transfer N_{fs} across each facet s described by Eqs. (11) and (12) is by no means small. However, the main short-wave contribution of these fluctuations to the microstructural evolution is self-averaging and is described by the diffusional term δN_{di}. Only the long-wave fluctuations with $l \gtrsim l_{le}$ remain meaningful for this term and should be taken into account in the calculations.

To describe this physical picture, we suggest the following model. Instead of the full stochastic quantities $N_i(t)$ and δN_{fi} in Eq. (10), we consider only their long-wave parts, $N_i^c(t)$ and δN_{fi}^c, which are determined by a "coarse-grained" version of Eq. (10):

$$N_i^c(t + \delta t) = N_i^c(t) + \delta N_{di}\{c_j\} + \delta N_{fi}^c. \quad (13)$$

Here, the local concentration c_j in the diffusional term δN_{di} is $N_j^c(t)/N_L$, while the last term is the sum of coarse-grained fluctuative transfers δN_{fs}^c across all facets s: $\delta N_{fi}^c = \sum_s \delta N_{fs}^c$. This transfer δN_{fs}^c is obtained from the full stochastic distribution δN_{fs} determined via Eqs. (11) and (12) by a "filtration of noise" procedure, that is, by introducing a proper cutoff factor $F_c(\mathbf{k})$ in the Fourier-component $\delta N_{f\alpha}(\mathbf{k})$ of the full function $\delta N_{fs} = \delta N_{f\alpha}(\mathbf{R}_{s\alpha})$, where $\mathbf{R}_{s\alpha}$ stands for the center of the facet s normal to the main crystal axis α:

$$\delta N_{f\alpha}^c(\mathbf{R}_{s\alpha}) = \sum_{\mathbf{k}} \exp(-i\mathbf{k}\mathbf{R}_{s\alpha})\delta N_{f\alpha}(\mathbf{k})F_c(\mathbf{k}), \quad (14)$$

$$\delta N_{f\alpha}(\mathbf{k}) = \frac{1}{N_{tot}}\sum_{\mathbf{R}_{s\alpha}} \exp(i\mathbf{k}\mathbf{R}_{s\alpha})\delta N_{f\alpha}(\mathbf{R}_{s\alpha}), \quad (15)$$

and N_{tot} is the total number of L cells. The cutoff factor $F_c(\mathbf{k})$ is taken in a Gaussian-type form characterized by the cutoff length l_c or by the parameter $g_c = l_c/L$:

$$F_c(\mathbf{k}) = \exp\left[-2g_c^2\sum_\alpha \sin^2(k_\alpha L/2)\right]. \quad (16)$$

Here, we took into account that the set of arguments $\mathbf{R}_{s\alpha}$ of the function $\delta N_{f\alpha}^c(\mathbf{R}_{s\alpha})$ forms a cubic crystal of L cells, and so the Fourier component $\delta N_{f\alpha}^c(\mathbf{k})$ should obey the following relations: $\delta N_{f\alpha}^c(k_\beta + 2\pi/L) =$

$\delta N^c_{f\alpha}(k_\beta)$. For the large $g^2_c \gg 1$ used below, cutoff function (16) is effectively reduced to a Gaussian $\exp(-k^2 l^2_c/2)$.

The cutoff length l_c for our problem should evidently have the order of a characteristic length of a local equilibrium, l_{le}, as the phase separation process can take place only when a sufficient thermodynamic driving force (i.e., supersaturation) is present, which implies a certain extent of the local thermodynamic equilibrium within a subsystem. At the same time, all fluctuations with larger wavelengths $l \gtrsim l_{le}$ can initiate this process and, thus, should be taken into account. The length l_{le} should generally depend on the concentration c, temperature T, and the interaction radius r_0 in (8). To estimate the l_{le} value, we made computer simulations of phase separation based on Eqs. (13)–(16) for a number of values of c, T, r_0 while varying the parameter $g_c = l_c/L$ in Eq. (16). In accordance with the considerations above, the decreasing of l_c from the values $l_c > l_{le}$ to $l_c < l_{le}$ should correspond to the loss of the local equilibrium assumed in Eqs. (2)–(6) and, thus, to sharp violations of the basic condition $\lambda_i \simeq \mathrm{const}$ within subsystems. The scale of these violations can be characterized, for example, by the "degree of nonequilibrium" $I_m(l_c)$ defined as the maximum value of the reduced gradient $\beta a |\nabla\lambda|_{\max}$ over the whole system for some characteristic time interval Δt_c. Then, decreasing l_c across l_{le} should result in a sharp rise of $I_m(l_c)$. This is illustrated in Fig. 1, and similar variations have been found for all other models considered. The point l_{sr} where this sharp rise starts can be defined, for example, as the maximum curvature point for the function $I_m(l_c)$. The local equilibrium length l_{le} should evidently somewhat exceed the l_{sr} value. The experience of our simulations seems to show that employing $l_c = l_{le} \simeq 2l_{sr}$ usually provides an appropriate description of evolution, while varying l_c, say, between $2l_{sr}$ and $1.5l_{sr}$ results mainly in some rescaling of time and only slight changes in the microstructure; it is illustrated by a comparison of frames (b) and (e) to (g) and (h) in Fig. 3 below.

We used equations (11)–(16) with the above-described choice of l_c in (16) to simulate phase separation for a number of alloy models with different c, T, and r_0 values. Some of our results are presented in Figs. 2 and 3. They correspond to 2D simulation on the FCC lattice with 256×256 L cells and periodic boundary conditions. The concentration c is 0.4, while the reduced temperatures $T' = T/T_c$ are chosen near the spinodal temperature for this c, namely, $(T'_s)_{\mathrm{MFA}} = 0.96$. These c and T'_s values are close to those used in experiments [5], where the NG–SD transition was studied for some highly viscous liquid mixture, and so our results can be directly compared to this experiment. All simulations included a "preannealing" stage at $T'_{an} = 1.2$ for
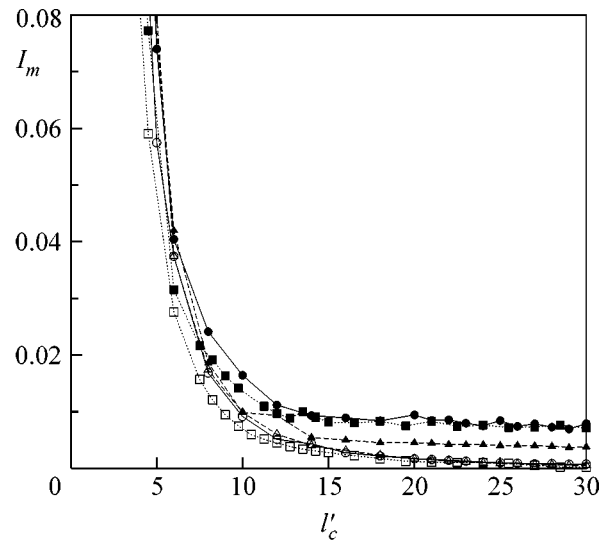

Fig. 1. The inhomogeneity parameter I_m described in the text versus the reduced cutoff length $l'_c = l_c/a$ at $L = 2a$, $\Delta t'_c = 5$, and $c = 0.4$. Closed and open symbols correspond to the reduced temperatures $T' = 0.94$ and $T' = 0.98$, while circles, triangles, and squares correspond to $r_0 = a$, $r_0 = 2a$, and $r_0 = 0.71a$, respectively.
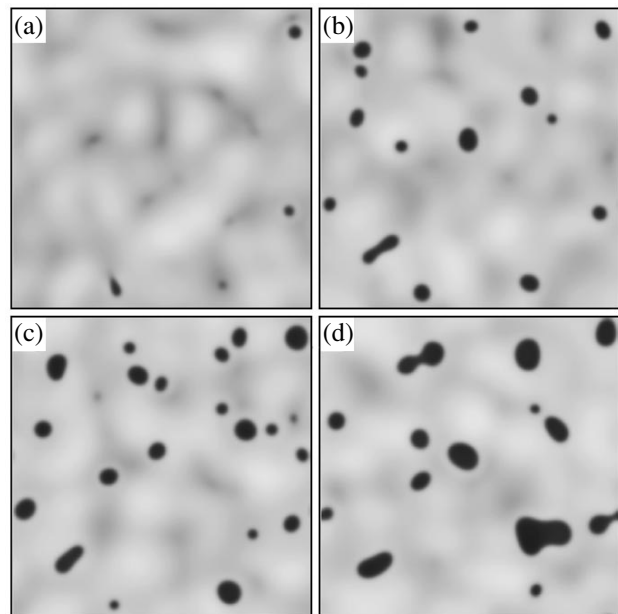

Fig. 2. Temporal evolution of $c_i = c(\mathbf{R}_i)$ for the alloy model described in the text at $L = 2a$, $c = 0.4$, $r_0 = a$, $T' = 0.98$, $l'_c = 26$, and the following $t' = r\gamma_{nn} \times 10^{-4}$: (a) 2, (b) 5, (c) 10, and (d) 25. The gray level linearly varies with c_i between $c_{\min} = 0.3$ and $c_{\max} = 0.65$ from completely bright to completely dark.
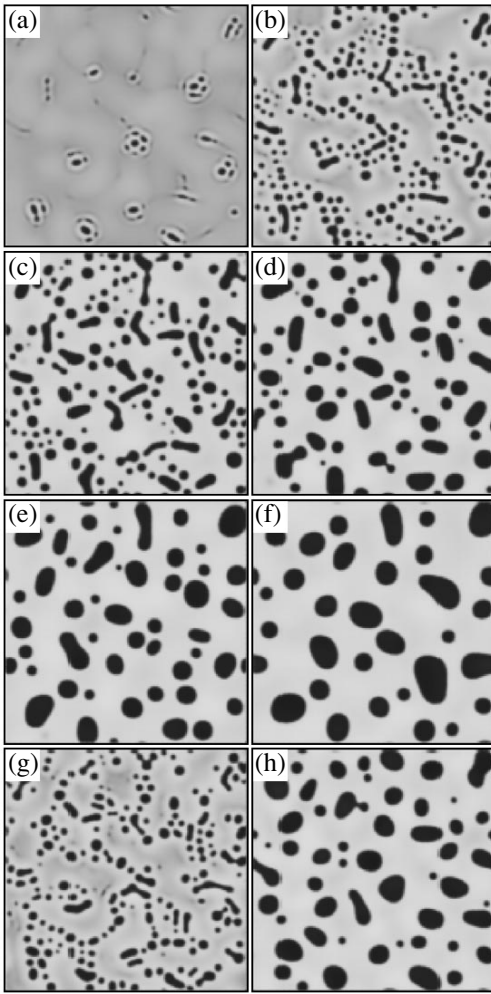
Fig. 3. (a–f) Same as in Fig. 2 but at $T' = 0.94$, $c_{min} = 0.25$, $c_{max} = 0.75$, and the following t': (a) 0.5, (b) 1, (c) 2, (d) 5, (e) 10, and (f) 20. (g, h) Same as in frames (a)–(f) but at $l'_c = 20$ and the following t': (g) 0.7 and (h) 7.

the interval $\Delta t'_{an} = 0.05$, where $t' = t\gamma_{nn} \times 10^{-4}$ is the reduced time, while the symbol t' in figure captions shows the time after a rapid quench $T'_{an} \longrightarrow T'$.

The patterns presented in Figs. 2 and 3 reveal all main features of phase separation of the NG and the SD type, respectively, as mentioned, e.g., by Tanaka *et al.* [5]. Discussing their observations, these authors note that "in NG the nuclei… are born and grow almost independently. The density of droplets in NG is much lower than in SD. In SD the spatial-concentration fluctuations grow in both amplitude and size and form droplets, being first gray, become darker with time, and become larger and larger mainly by coalescence mechanism." All these features are seen in Figs. 2 and 3.

The simulations also reveal a number of other microstructural details. In particular, for the NG-type

evolution shown in Fig. 2 note the following: (i) some rare coalescence events are present as well; (ii) the precipitate shape is often nonspherical; and (iii) a concentration-depleted "bright" halo is typically adjacent to the precipitates. All of these seen in experiments [4, 5]. For the SD-type evolution in Fig. 3, we observe the following: (i) peculiar initial "roelike" arrays of droplets, which later often coalesce, forming elongated tonguelike structures, and (ii) many coalescence events occur via a "bridge" mechanism noted in [12], when the diffusion fluxes first connect the adjacent precipitates by a thin gray "bridge" that later starts to sharply grow and thicken with the formation of a pearlike or a dumbbelllike precipitate. It again agrees with experiments [5, 6].

In our simulations, for the transition region between NG and SD, in particular, for $c = 0.4$, $T' = 0.96$ just at the spinodal curve, we obtain a "mixed" type of evolution: first an NG-type pattern of a small number of wrong-shaped droplets, which later form roelike and tonguelike structures characteristic of SD. It seems to agree with the observations described in [5].

Finally, we comment on the smallness of the temperature width for the NG–SD transition illustrated by Figs. 2 and 3: $\Delta T' \simeq 0.04$. It can be explained by the significant difference in the reduced supersaturation parameter for the alloy states c, T considered. This parameter characterizes a tendency in the NG or the SD-type evolution and can be defined as [10]

$$s = [c - c_b(T)]/[c_b(T) - c_s(T)], \qquad (17)$$

where $c_b(T)$ and $c_s(T)$ are the concentration at the binodal and the spinodal, respectively. For the two states considered, this parameter takes quite different values, namely, $s_1 = 0.42$ and $s_2 = 1.27$, even though the temperature difference is small. It is due to the flatness of the binodal and the spinodal curves, $T_b(c)$ and $T_s(c)$, in the vicinity of the critical point being considered in this simulation. It can be still more so for experiments [5], where the curves $T_b(c)$ and $T_s(c)$ seem to be still flatter than in our MFA model; it can explain a rather small value of the NG–SD transition width, $\Delta T' \simeq 0.015$, found in [5].

REFERENCES

1. K. Binder, in *Materials Science and Technology*, Vol. 5: *Phase Transformations in Materials*, Ed. by P. Haasen (VCH, Weinheim, 1991), Chap. 7.
2. R. Wagner and R. Kampmann, in *Materials Science and Technology*, Vol. 5: *Phase Transformations in Materials*, Ed. by P. Haasen (VCH, Weinheim, 1991), Chap. 4.

3. K. Oki, H. Sagane, and T. Eguchi, J. Phys. Colloq. **38**, C7-414 (1977).

4. F. Ernst and P. Haasen, Phys. Status Solidi A **104**, 1702 (1994).

5. H. Tanaka, T. Yokokawa, H. Abe, *et al.*, Phys. Rev. Lett. **65**, 3136 (1990).

6. H. Tanaka, Phys. Rev. Lett. **72**, 1702 (1994).

7. L. D. Landau and E. M. Lifshitz, *Course of Theoretical Physics*, Vol. 5: *Statistical Physics*, 4th ed. (Nauka, Moscow, 1995; Butterworth, London, 1999), Sect. 162.

8. J. W. Cahn, Acta Metall. **9**, 795 (1961).

9. F. Soisson and G. Martin, Phys. Rev. B **62**, 203 (2000).

10. V. Yu. Dobretsov and V. G. Vaks, J. Phys.: Condens. Matter **10**, 2261 (1998); **10**, 2275 (1998).

11. J. G. Amar, F. E. Sullivan, and R. D. Mountain, Phys. Rev. B **37**, 196 (1988).

12. V. G. Vaks, S. V. Beiden, and V. Yu. Dobretsov, Pis'ma Zh. Éksp. Teor. Fiz. **61**, 65 (1995) [JETP Lett. **61**, 68 (1995)].

13. Y. Wang, D. Banerjee, C. C. Su, and A. G. Khachaturyan, Acta Mater. **46**, 2983 (1998).

14. V. G. Vaks, Phys. Rep. **391**, 157 (2004).

15. N. G. van Kampen, *Stochastic Processes in Physics and Chemistry* (North-Holland, Amsterdam, 1984; Vysshaya Shkola, Moscow, 1986).

Electronic, Structural, and Thermal Properties of a Nanocable Consisting of Carbon and BN Nanotubes

A. N. Enyashin[1, 2], G. Seifert[1], and A. L. Ivanovskiĭ[2]

[1] *Institut für Physikalische Chemie, Technische Universität Dresden, D-01062 Dresden, Germany*
[2] *Institute of Solid-State Chemistry, Ural Division, Russian Academy of Sciences, Yekaterinburg, 620219 Russia*
e-mail: ivanovskii@ihim.uran.ru

The band structure and thermal behavior of a coaxial C/BN nanocable (5,5)C@(17,0)BN consisting of a carbon nanotube and a boron nitride nanotube have been studied using a tight-binding approximation based on density functional theory. The system is stable up to $T \sim 3500$–3700 K. As the temperature increases, deformations of the BN tube begin earlier than those of the carbon tube. The near-Fermi states of the nanocable are formed by the overlapping π–π^* bands of the carbon tube, and the outer BN nanotube (the nanocable sheath) is an insulator with a bandgap of ~4 eV. The electronic properties of the nanocable (the metallic-type conductivity of the C tube and the insulating character of the BN tube) are retained over the entire temperature interval. © *2004 MAIK "Nauka/Interperiodica".*

PACS numbers: 61.46.+w; 73.22.+i; 85.35.Kt

The idea of creating a nanocable (a nanoscale conductor covered with an insulating sheath) as a functional element of various electronic nanodevices arose soon after the synthesis of carbon nanotubes [1] and the studies of their properties in [2, 3]. Multilayer carbon nanotubes, where the inner and outer tubes must possess metallic-type and semiconductor-type conductivities, respectively, were suggested as the first prototype nanocable. In spite of their seeming simplicity, attempts to create such cables, that is, to synthesize sufficiently extended carbon multilayer nanotubes with the controlled conductivity of coaxial carbon cylinders, have failed so far.

Certain success in the design of purely carbon nanocables was achieved in 2004: the authors of [4] obtained a bicable (two parallel carbon nanotubes enclosed in a common sheath) as a product of the coalescence of two bilayer C nanotubes. However, the problem of controlling the conducting properties of each C nanotube entering into such a system also remains open.

Progress in the synthesis of a large group of novel nanotubes based on a number of inorganic materials (see reviews [5, 6]) has substantially extended the possibilities of selecting nanotubes as elements of a nanocable. It turned out that boron nitride nanotubes (BN nanotubes) can serve as the most favorable insulating cable sheath. Stable dielectric properties are their unique feature: the bandgap of BN nanotubes remains sufficiently stable (in the range 4–5 eV) regardless of their diameter and chirality [5, 6]. Thus, the method of filling these tubes with a metallic nanowire becomes

the main problem in manufacturing a cable with a BN nanotube sheath.

The first suggestions on the formation of the desired nanowire were reduced to the intercalation of metal atoms (for example, K or Al [7]) into a BN nanotube. In spite of encouraging predictions, attempts at synthesizing such heterosystems have not met with real success [8]. An alternative solution is the synthesis of a nanocable *in situ* by the substitution method, in which a carbon multilayer nanotube is used as a starting system and the boron nitride sheath is formed upon the substitution of boron and nitrogen atoms for carbon atoms in the outer C nanotube. Samples of mixed boron carbon nitride (B–C–N) tubes with a layer-by-layer gradient of the C/BN concentration, which ensures a semiconducting type of the inner B–C–N tubes and an insulating type of the outer BN nanotube, have been obtained by this method [9].

The growth of a nanocable from so-called bunker phases, which represent an assembly of fullerenes encapsulated in a bunker (nanotube), may become a radically different method of solving the problem. It is known that, under certain conditions (for example, under irradiation with a flux of high-energy particles), one can stimulate the polymerization of fullerenes according to the following scheme: fullerenes ⟶ prolate nanocapsules ⟶ nanotube to obtain tubular systems in which the diameter of the inner tube growing from fullerene molecules is strictly controlled by the size of the outer BN tube.

Recent experiments [10] have shown that unique C/BN heterosystems, namely, carbon nanotubes inside BN nanotubes, can be obtained by this method. These

Cell sizes and compositions, bandgap for the nanotubes and the nanocable, and effective atomic charges as functions of temperature

System	Cell (number of atoms)		Bandgap, eV
(5,5) C nanotube	180 (C)		Metal
(17,0) BN nanotube	340 (170 B + 170 N)		4.05
(5,5)C@(17,0)BN	520 (180 C + 170 B + 170 N)		Metal
Temperature	Atomic charges for (5,5)C@(17,0)BN		
	Q(C)	Q(B)	Q(N)
0 K	0	+1.342	−1.342
1000 K	−0.006…+0.040	+1.303…+1.436	−1.497…−1.245
3000 K	−0.214…+0.124	+1.326…+1.705	−1.922…−1.125

results raise a number of important questions: (i) What is the band structure of such tubular C/BN heterosystems and how does it correspond to the concept of the electronic properties of a nanocable? (ii) What are the structural properties and thermal stability of C/BN systems? (iii) How do the electronic properties of C/BN systems change upon thermal treatment?

This work presents the first results of *ab initio* calculations of the band spectrum and structural and thermal properties of a nanotubular C/BN heterostructure considered as a prototype nanocable.

It is known that all armchair (n,n)C nanotubes exhibit metallic conductivity [3]. Therefore, coaxial tubes were taken as the starting nanocable model: an armchair (5,5)C nanotube inside a zigzag (17,0)BN tube (sheath) (a (5,5)C@(17,0)BN nanotube, Fig. 1). The starting atomic models of the C and BN tubes and the nanocable were constructed by the standard procedure of rolling a graphite network or a hexagonal boron nitride network into seamless cylinders [3]. Their diameters were calculated by the known expression $D = (a/\pi)\sqrt{(n^2 + nm + m^2)^{1/2}}$, where n and m are chiral indices and a is the C–C or B–N bond length in planar networks. The diameters of the chosen C and BN nanotubes were 0.679 and 1.332 nm, respectively. This corresponded to the distance between the walls of the coaxial tubes in the nanocable, 0.327 nm, which was close to the van der Waals gap in the synthesized multilayer nanotubes [2, 3]. The atomic sizes of the tube and nanocable cells are given in the table, and their translation parameter equals 2.175 nm.

At the first stage, the full geometry optimization of the nanocable was performed (at $T = 0$ K) and its electronic structure was investigated. Next, we performed a simulation of the thermal deformation of the nanocable structure in the range $T = 0$–4000 K and carried out band calculations of electronic spectra at various temperatures for the obtained structural forms of the nanocable.

The calculations were performed using a self-consistent charge-density-functional-based nonorthogonal

tight-binding (SCC-DFTB) scheme [11]. An atomic *sp* basis set was used, and the calculations of the Hamiltonian and matrix elements were performed within density functional theory using the local density approximation. The starting atomic geometry of the nanotubes was fully optimized with respect to the atomic positions and the cell length using a gradient scheme. The thermal behavior of the nanocable was simulated by the molecular dynamics method within the DFTB scheme (the deMon program package) [12].

In the optimized structure of the perfect nanocable ($T = 0$ K), the C-nanotube diameter is 6.88 nm and the C–C bond lengths are 0.1416 and 0.1414 nm across and
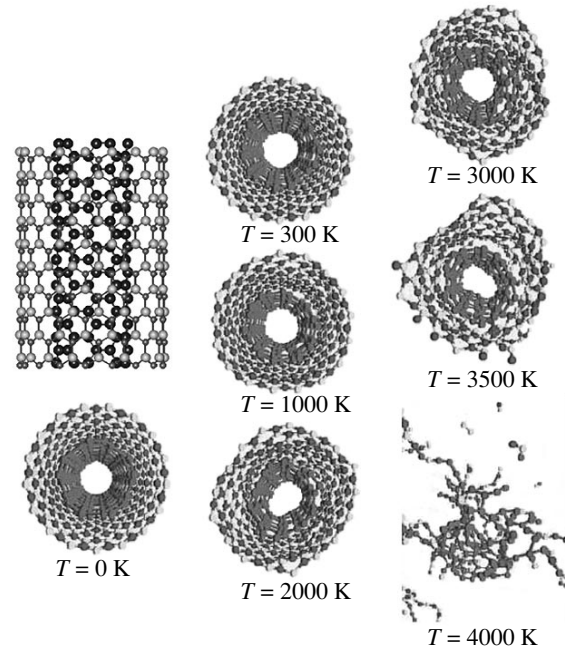

Fig. 1. Structure of the C(5,5)@BN(17,0) nanotube (side and top views at $T = 0$ K) and its distortions at various temperatures.
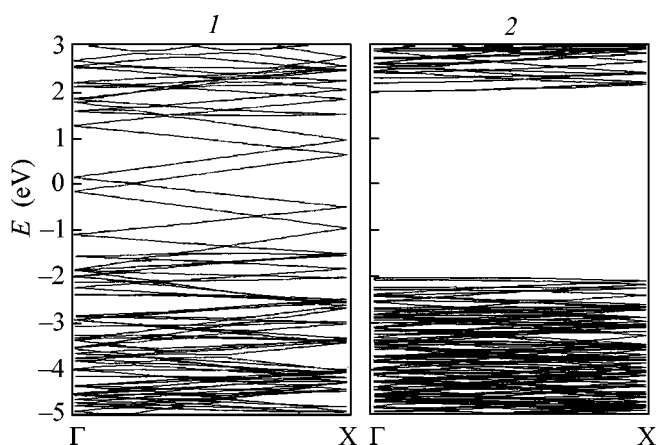
Fig. 2. Energy bands for (a) (5,5)C nanotube and (b) (17,0)BN nanotube. Horizontal lines at 0 eV correspond to the Fermi level.

along the tube axis, respectively. The wall of the boron nitride tube bloats in such a way that the boron and nitrogen atoms undergo radial displacements (with respect to their positions in the BN cylinder) toward (B) and away from (N) the tube center. The effect is associated with the electrostatic interaction of atoms; according to our DFTB calculations, the charge polarization between atoms B←→N is 1.342 e. As a result, the diameters of the oppositely charged boron and nitrogen cylinders in the BN nanotube are 1.362 and 1.370 nm,

respectively. Note that similar relaxation effects occur in pure boron nitride nanotubes [13, 14]. Along with radial deformations, anisotropy of the B–N bond lengths is observed for the BN tube, namely, 0.1454 and 0.1451 nm across and along the tube axis, respectively.

The results of the molecular-dynamics simulation of the thermal deformations of the nanocable are illustrated in Fig. 1. It is evident that the nanocable structure under ambient conditions ($T = 300$ K) remained virtually unchanged as compared to the perfect structure ($T = 0$ K). Deformations become appreciable in the range 1000–2000 K, and they rapidly progress up to 3500 K. In the range 3500–4000 K, the cable is destroyed. It is important to emphasize that the inner carbon tube exhibits higher thermal stability and the BN sheath of the cable is destroyed first. This is explained by a number of factors. First, the interatomic interaction energy for strong covalent C–C bonds is larger than that for B–N bonds, which are characterized by a notable ionic component. This determines the extreme thermomechanical characteristics of C nanotubes [14]. Second, rehybridization defects and topological defects (Stone–Wales type, see [3, 6]) form in the C nanotube with increasing temperature; the cylindrical morphology is retained in this case. Such defects (when some heteropolar B–N bonds transform into significantly less stable homopolar B–B and N–N bonds) are less typical for BN tubes [15].
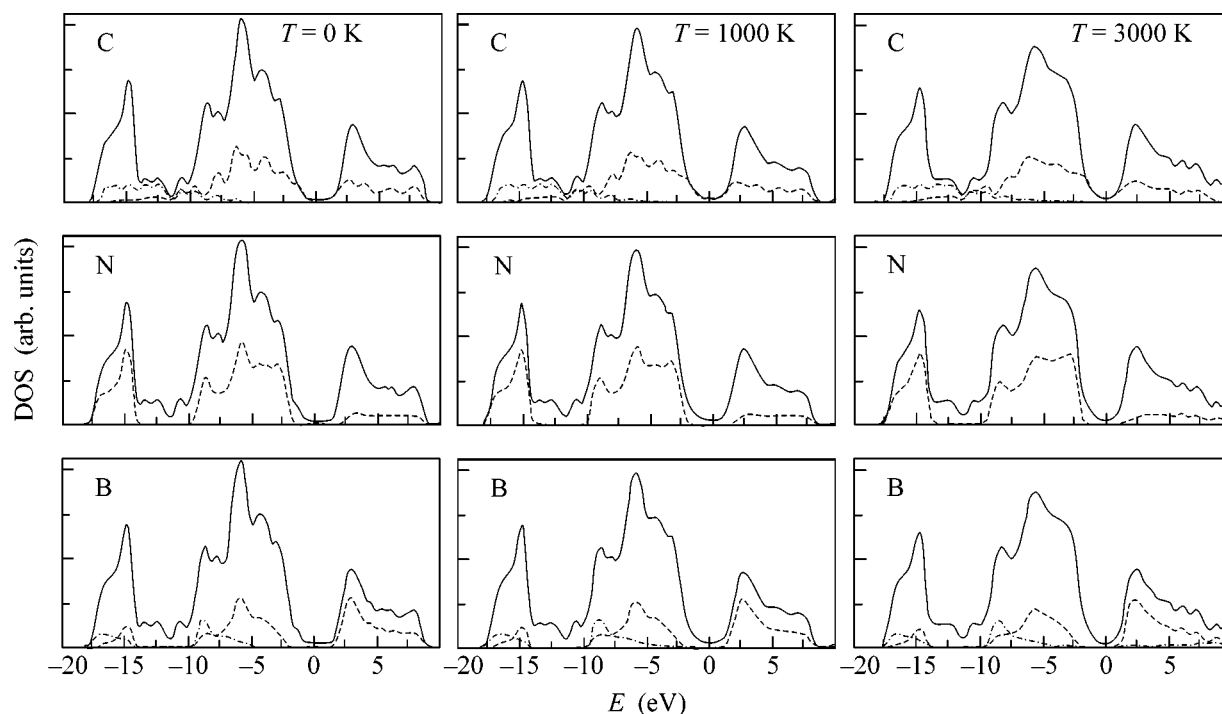

Fig. 3. (Solid lines) Total and (dashed lines) $2p$ and (dotted lines) $2s$ partial densities of states of (from top to bottom) carbon, nitrogen, and boron according to band DFTB calculations for C(5,5)@BN(17,0)-nanocable structures at $T =$ (from left to right) 0, 1000, and 3000 K.

The energy bands of the isolated armchair (5,5)C nanotube and zigzag (17,0)BN nanotube are shown in Fig. 2. The electronic states of the C nanotube at the Fermi level (E_F) are determined by π and π^* band crossing in the direction of the tube axis ($\Gamma \longrightarrow X$), leading to the metallic-type spectrum. On the contrary, the zigzag (17,0)BN tube is an insulator with a bandgap of 4.05 eV (direct transition at the Γ point). In this case, the highest occupied and lowest vacant bands are composed of N$2p(\pi)$ and B$2p(\pi^*)$ states.

The total and partial densities of states (DOSs) of the nanocable at $T = 0$, 1000, and 3000 K are given in Fig. 3. It is evident that the band spectrum of the perfect heterosystem (the (5,5)C@(17,0)BN nanotube) at $T = 0$ is close to a superposition of the spectra of isolated C and BN tubes: (i) DOSs at E_F (from –2.5 to +1.5 eV) are formed exclusively by C$2p$ states; (ii) a bandgap of about 4 eV exists between the occupied and vacant bands of the BN tube; (iii) the highest occupied and lowest vacant bands of the BN tube are composed of N$2p$ and B$2p$ orbitals. Thus, the interactions between the states of the coaxial carbon and BN tubes are insignificant, and the C/BN heterostructure corresponds to the electronic properties required for a nanocable.

As thermal structural deformations grow, the charge states of atoms and the band spectrum of the nanocable exhibit a number of changes. Thus, the deviations of the positions of atoms from their perfect positions in the cable walls start at $T = 1000$ K and lead to the anisotropy of the charge states of nonequivalent B, C, and N atoms. This anisotropy reaches appreciable values at 3000 K, namely, up to ~27 and 42% for boron and nitrogen atoms, respectively. The charge states of the C atoms also become polarized (see table).

Figure 3 demonstrates that the amorphization of cable walls favors the characteristic smoothing of the DOS profile, while the energy positions of the main energy bands and their sequence in the nanocable spectrum remains unchanged. The band structure at the Fermi level, which is exclusively determined by the C$2p$ states of the carbon tube, also retains its general features. The conducting (metallic) properties of the carbon tube also remain unchanged. Moreover, the thermal defects forming in the walls (pentagon–heptagon type) lead to a certain increase in the density of states at the Fermi level (Fig. 3), that is, enhance the metallic character of the C tube. It is also important to note that no new bands arise in the bandgap region upon thermal deformations of the BN tube; thus, the BN nanotube retains its dielectric character. The main thermal effect is the smearing of the N$2p$ and B$2p$ band edges at the Fermi level in the BN tube and a decrease in the bandgap (down to ~2.4 eV at $T = 3000$ K).

Thus, the electronic and structural properties of a C/BN nanocable—a tubular coaxial heterosystem composed of a carbon nanotube and a boron nitride nanotube—have been studied by an *ab initio* band structure DFTB method, and the variations of these properties in the temperature range 0–4000 K have been examined. It has been found that the nanocable band structure is formed by slightly hybridized states localized on atoms of the outer (BN) and inner (carbon) nanotubes. The conducting characteristics of the system (metallic for the carbon nanotube and dielectric for the outer BN tube serving as the cable sheath) are retained in the entire temperature range of heterosystem stability (up to $T \sim 3500$–3700 K). The main effect of temperature increase is a change in the bandgap width of the BN nanotube as a result of the band-structure modification upon the thermal deformations of the atomic structure of the walls. This permits the suggestion that a thermal treatment of the C/BN nanocable may become a promising method for controlling its electrophysical characteristics.

REFERENCES

1. S. Iijima, Nature **354**, 56 (1991).
2. K. Tanaka, T. Yamabe, and K. Fuku, *The Science and Technology of Carbon Nanotubes* (Elsevier, Oxford, 1999).
3. P. J. F. Harris, *Carbon Nanotubes and Related Structures: New Materials for the Twenty-First Century* (Cambridge Univ. Press, Cambridge, 1999).
4. M. Endo, T. Hayashi, H. Muramatsu, *et al.*, Nano Lett. **4**, 1451 (2004).
5. R. Tenne, Prog. Inorg. Chem. **50**, 269 (2001).
6. A. L. Ivanovskiĭ, Usp. Khim. **71**, 203 (2002).
7. A. Rubio, Y. Miyamoto, X. Blasé, *et al.*, Phys. Rev. B **53**, 4023 (1996).
8. D. Golberg, F. F. Xu, and Y. Bando, Appl. Phys. A **76**, 479 (2003).
9. D. Golberg, P. S. Dorozhkin, Y. Bando, *et al.*, Appl. Phys. Lett. **82**, 1275 (2003).
10. W. Mickelson, S. Aloni, W.-Q. Han, *et al.*, Science **300**, 467 (2003).
11. D. Porezag, Th. Frauenheim, Th. Kohler, *et al.*, Phys. Rev. B **51**, 12947 (1995).
12. A. M. Koster, G. Geudtner, A. Goursot, *et al.*, National Research Council, Canada (2002).
13. E. Hernandez, C. Goze, P. Bernier, and A. Rubio, Phys. Rev. Lett. **80**, 4502 (1998).
14. B. Akdim, R. Pachter, X. Duan, and W. W. Adams, Phys. Rev. B **67**, 245404 (2003).
15. W. H. Moon and H. J. Hwang, Nanotechnology **15**, 431 (2004).

Translated by A. Bagatur'yants

Observation of Hubbard Bands in γ-Manganese[¶]

S. Biermann[1], A. Dallmeyer[1], C. Carbone[1], W. Eberhardt[1], C. Pampuch[2], O. Rader[2],
M. I. Katsnelson[3], and A. I. Lichtenstein[3]

[1] *Institut für Festkörperforschung, Forschungszentrum Jülich, D-52425 Jülich, Germany*
[2] *BESSY, D-12489 Berlin, Germany*
[3] *University of Nijmegen, NL-6525 ED Nijmegen, The Netherlands*
e-mail: biermann@cpht.polytechnique.fr; A.Lichtenstein@sci.kun.nl
Received October 13, 2004

We present angle-resolved photoemission spectra of the γ phase of manganese as well as a theoretical analysis using a recently developed approach that combines density functional and dynamical mean-field methods (LDA + DMFT). The comparison of experimental data and theoretical predictions allows us to identify effects of the Coulomb correlations, namely, the presence of broad and nondispersive Hubbard bands in this system. © 2004 MAIK "Nauka/Interperiodica".
PACS numbers: 71.15.Qe; 71.20.Be; 79.60.–i

The electronic theory of metals is based on the concept of quasiparticles, elementary excitations in the many-electron system that show a one-to-one correspondence with noninteracting electrons. However, strong electronic correlations can destroy this picture and result in the formation of so-called Hubbard bands of an essentially many-body nature [1]. This concept is crucial for modern theories of strongly correlated electron systems [2]. The formation of Hubbard bands takes place, e.g., in many transition metal–oxide compounds, which thus have to be viewed as Mott insulators or doped Mott insulators [3]. Transition metals represent another class of systems where many-body effects are important (see [4] and references therein). However, according to common belief, they are moderately correlated systems and normal Fermi liquids.

Electronic spectra of transition metals have been probed intensively by angle-resolved photoemission, a technique that allows for the determination of the dispersion law that describes the dependence of the quasiparticle energy on quasimomentum. Copper was the first metal to be investigated thoroughly by this technique, and the results were in excellent agreement with band structure calculations [5, 6]. The same technique, however, showed substantial deviations when applied to Ni and provided evidence for many-body behavior, such as the famous 6-eV satellite [7, 8]. The quasiparticle damping in iron can be as large as 30% of the binding energy [9, 10]. Correlation effects are indeed important for metals with partially filled 3*d* bands and should be taken into account for an adequate description of ARPES spectra. Nevertheless, the main part of the spectral density in Fe is related to usual quasiparticles, and the spectral weight of the satellite in Ni

amounts to only 20% [10]. In the present letter, we provide evidence for surprisingly strong correlation effects in the fcc-(γ) phase of manganese, which are much stronger than in other transition metals.

Investigations of an extended Hubbard model show that correlation effects are strongest for half-filled *d* bands [11]. Normally, the geometrical frustrations in crystals (such as in the fcc lattice) further enhance electronic correlations [2], so that one of the best candidates among the transition metals for the search for strong correlation effects is the fcc-(γ) phase of manganese. It is an example of a very strongly frustrated magnetic system; according to band-structure calculations [12], the antiferromagnetic ground state of γ-Mn lies extremely close to the boundary of the nonmagnetic phase. Moreover, an anomalously low value of the bulk modulus [13] might be considered as a first experimental hint of strong electronic correlations.

The physical properties of bulk γ-Mn are hardly accessible in the experiment, since the γ-phase is only stable at temperatures between 1368 and 1406 K, where it shows paramagnetic behavior. Thin films of γ-Mn, however, can be stabilized by epitaxial growth on $Cu_3Au(100)$ [14], which has an interatomic spacing (2.65 Å) very close to the interatomic spacing of Mn-rich alloys (2.60–2.68 Å). Schirmer *et al.* [14] have shown that $Cu_3Au(100)$ supports layer-by-layer growth at room temperature up to coverages of 20 monoatomic layers (ML). A low-energy electron diffraction (LEED) *I*(*V*) analysis revealed that the Mn films adopt the in-plane spacing of the $Cu_3Au(100)$ substrate and a comparatively large tetragonal distortion of the fcc lattice. For the inner layers of a 16-ML Mn film, this distortion amounts to –6%, whereas the surface–subsurface distance is very close to the Cu_3Au value.

[¶] This article was submitted by the authors in English.

We have used angle-resolved photoemission at the undulator beamline TGM-5 and on the TGM-1 beamline at BESSY at a combined energy resolution of 250 meV to probe the electronic states in γ-Mn. The $Cu_3Au(100)$ substrate was prepared by repeated cycles of Ne^+ sputtering and annealing, until a very good LEED pattern with sharp diffraction spots and a low background intensity confirmed a high degree of structural order. The base pressure of 2×10^{-10} mbar rose to 7×10^{-10} mbar as Mn was deposited by electron beam evaporation. To avoid interdiffusion of Cu and Au, the onset of which was determined to be above room temperature [14], we kept the sample at room temperature during the Mn deposition and the photoemission measurements. We observe in all experiments LEED patterns of Mn/Cu_3Au of the (1×1) type and a quality comparable to those of Fig. 3 in [15].

Angle-resolved photoemission measures the electron spectral density $A(\mathbf{k}, E)$ as a function of the quasi-momentum $\mathbf{k}$ and the energy E multiplied by the Fermi distribution function $f(E)$ [16]. For a given photon energy and electron emission angle corresponding to a certain $\mathbf{k}$ in the photoemission initial state, the spectral density usually has a well-defined maximum as a function of E that determines the quasiparticle dispersion $E(\mathbf{k})$ for the occupied part of the electronic bands. Figure 1 shows experimental data obtained for γ-Mn at a photon energy of 34 eV. This energy was chosen to follow the [111] direction (Γ–L) as closely as possible starting out near Γ at 0° and reaching L around a 30° electron emission angle. The spectra are characterized by two striking features. These are a weakly dispersive quasiparticle band near the Fermi level E_F and a broad and almost $\mathbf{k}$-independent maximum at approximately 2.7 eV below E_F. These structures lack a significant dispersion also in spectra taken at normal electron emission corresponding to the [100] direction for photon energies from 14 eV (~0.3$\overline{\Gamma X}$) to 70 eV (~0.5$\overline{X\Gamma}$) in Fig. 2.

These data cannot be understood in the framework of a standard quasiparticle picture, since first principles calculations of the band structure for different magnetic phases of γ-Mn show an energy dispersion of more than 1.5 eV [17] (Fig. 4). Instead, the overall shape of the experimental spectra is very close to that of the Hubbard model on the metallic side of the Mott transition with a quasiparticle band near the Fermi level and a broad Hubbard band below E_F [18].

To test this hypothesis, we have carried out first principles (LDA + DMFT) calculations [19, 20] of the electronic structure of γ-Mn that include correlation effects in a local but fully dynamical approximation for the electron self-energy Σ, using the full Hamiltonian LDA + DMFT scheme described in [4] with U values between 3 and 5 eV and $J = 0.9$ eV. Carrying out between 10 to 15 DMFT iterations with about 10^5 quantum Monte Carlo sweeps [21] allows us to obtain not only the local Green's function $G(\tau)$ but also highly
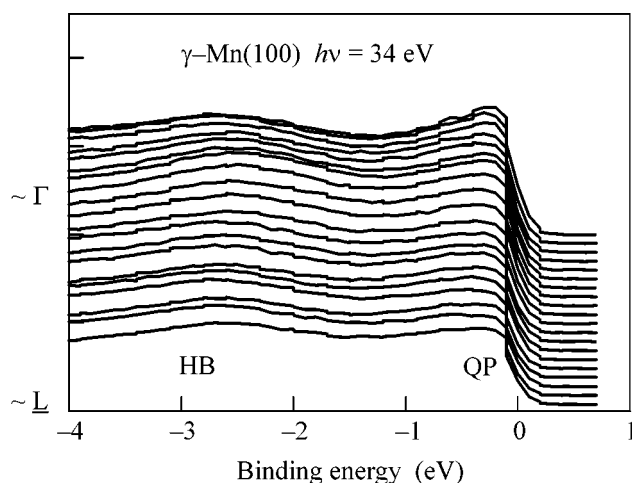

Fig. 1. ARPES spectra of bulklike γ-Mn (17 ML) taken at a photon energy of 34 eV for different electron emission angles corresponding approximately to $\mathbf{k}$ vectors between the Γ and the L points in the Brillouin zone; binding energies are measured with respect to the Fermi energy. This should be compared to the negative energy parts of the calculated spectra in Fig. 3.
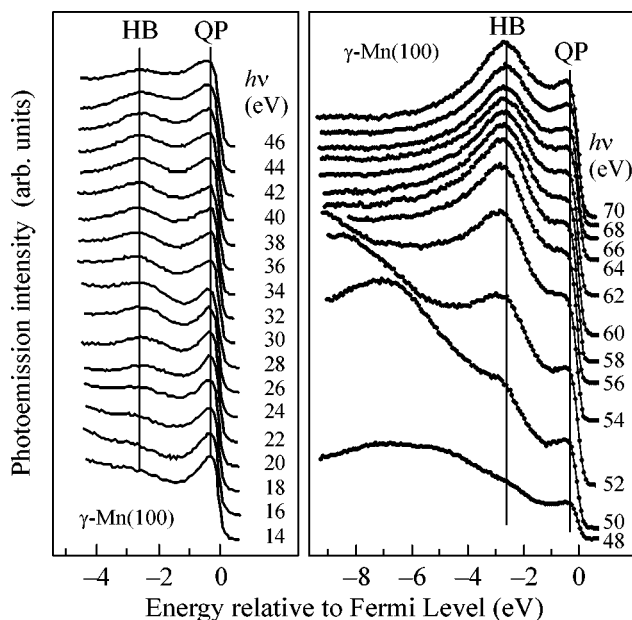

Fig. 2. ARPES spectra taken in normal emission at photon energies of 14 to 70 eV. The lack of dispersion distinguishes γ-Mn from other transition metals. The spectra are normalized to the photon flux. Note that the spectral changes from 48 to 52 eV are due to resonant transitions between 3p and 3d states.

accurate self-energies, which can then be used for the computation of the $\mathbf{k}$-resolved local Green's function

$$\hat{G}(\mathbf{k}, \tau)$$

$$= \frac{1}{\beta}\sum_n e^{-i\omega_n\tau}(i\omega_n + \mu - \hat{H}^{LDA}(\mathbf{k}) - \hat{\Sigma}(i\omega_n))^{-1}, \quad (1)$$
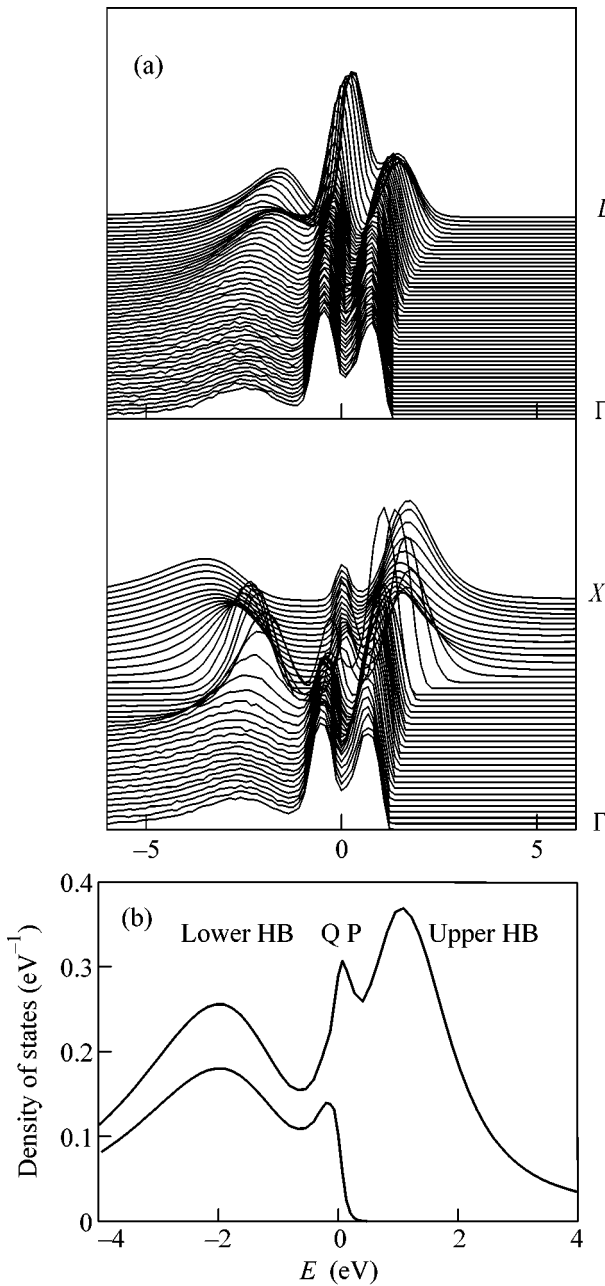
Fig. 3. Spectra calculated within the LDA + DMFT approach. (a) **k**-resolved density of states $A(\mathbf{k}, \omega)$ [arbitrary units]. The different curves correspond to k-points between the Γ and the L point and the Γ and the X point, respectively. (b) Angle-integrated spectral function. The "three-peak structure" with the two broad Hubbard bands (HB) and a narrow quasiparticle (QP) Kondo resonance at the Fermi level (solid line) is typical of strongly correlated systems. The calculated angle-integrated photoemission spectrum (dashed line), i.e., the density of states multiplied with the Fermi function and broadened with the experimental resolution, shows reasonable agreement with the experimental spectra.

where ω_n are the Matsubara frequencies corresponding to the inverse temperature $\beta \sim 0.002$ K^{-1} and H^{LDA} denotes an LDA–LMTO [22] *spd* Hamiltonian cor-
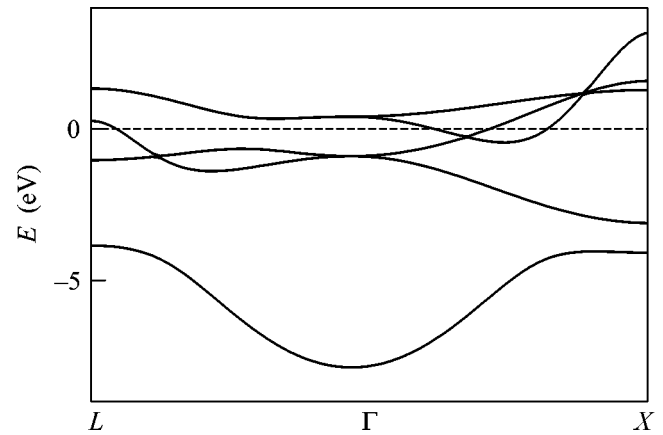

Fig. 4. Band structure of γ-Mn as calculated within density functional theory within the local density approximation (LDA).

rected for double counting of the Coulomb energy of the d states in the usual way [20]. Inversion of the spectral representations of the local Green's function and the dd block of the **k**-resolved one by means of a maximum entropy scheme [23] yields the density of states (DOS) $\rho(\omega)$ and the spectral function $A(\mathbf{k}, \omega)$. To our knowledge, these calculations are the first ones that determine the **k**-dependence of the spectral density for a material with d states from LDA + DMFT with a realistic five-band Coulomb vertex.

The results are shown in Fig. 3, displaying the local density of states (Fig. 3b) and the **k**-resolved spectral functions $A(\mathbf{k}, i\omega)$ for **k** points in the Γ–L and Γ–X directions, respectively. In the negative energy part (that is, for the occupied states) of all spectra, two main peaks carry (for a given k point) the main part of the spectral weight: a narrow quasiparticle (QP) feature near the Fermi level and a very broad Hubbard band (HB) (at about –2.4 eV). These features are shared between the experimental (Fig. 1) and theoretical curves. The stronger dispersion of the (still very broad) low-energy peak in the Γ–X direction can be traced back to d states that strongly hybridize with the s band in that region of energy and **k** space. In the photoemission spectra, these s-like bands are suppressed due to matrix element effects. Given that (i) the experiments are done at a somewhat lower temperature than the calculations, that (ii) we do not take into account matrix elements when interpreting the photoemission data, and that (iii) using the maximum entropy scheme for determining the spectral function, a quantity not directly measured within the quantum Monte Carlo simulations, introduces a further approximation, the theoretical spectra agree reasonably well with the experimental data (Figs. 1, 2). In Fig. 4, the Kohn–Sham eigenvalues taken from the LDA calculation are plotted. The absence of LDA bands in the energy region near E_F carrying most of the spectral weight around the Γ point is striking and underlines the necessity of a

proper many-body treatment as done in LDA + DMFT. Note that assuming antiferromagnetic order (of the type detailed below) would slightly shift the LDA bands. However, the antiferromagnetic LDA band structure displays a dispersion of more than 2 eV and could thus not explain the nondispersive photoemission feature.

The calculated (**k**-integrated and **k**-resolved) density of states curves (Fig. 2) demonstrate a characteristic "three-peak structure," with two broad Hubbard bands and a narrow quasiparticle Kondo resonance at the Fermi level, which is typical of strongly correlated electron systems [2]. The quasiparticle peak at the Fermi level and the lower Hubbard band are seen in the present ARPES spectra; in **k**-unresolved (BIS) measurements [24], a broad peak has been observed at 1.4 eV. To identify this peak with the upper Hubbard band (located at 1.2 eV in our calculations), one should prove the dispersionless nature of this peak. We have checked that all these incoherent features do not depend on the directions in **k** space used in our calculations. For the above reasons, we believe that γ-Mn belongs to the class of strongly correlated materials and that the ARPES data can be considered as the first observation of Hubbard bands in a transition metal.

The energy scale associated with the correlation effects that lead to the formation of the Hubbard bands (~U) is much larger than that of the magnetic interactions. Therefore, the observed effects are not very sensitive to long-range magnetic order. We have carried out the electronic-structure calculations for both the paramagnetic and the antiferromagnetic structure with the wave vector $Q = (\pi, 0, 0)$, which is typical of γ-Mn-based alloys [25]. The magnetic ordering changes the electron spectrum little in comparison with the nonmagnetic case. However, in comparison with the results of standard band theory [12], the correlation effects stabilize the antiferromagnetic structure, thus leading to a magnetic moment of about 2.9μ_B.

According to the present results, γ-Mn can be considered a unique case of a strongly correlated transition metal. An even larger correlation would transform the system to a Mott insulator, where every atomic multiplet forms its own narrow but dispersive Hubbard band [1, 3]. On the other hand, in most metals, correlations are small enough for the quasiparticles to be well defined in the whole energy region, and usual band theory gives a reasonable description of the energy dispersion. Note that the correlation strength and bandwidth have almost the same magnitude for all 3d metals; γ-Mn is probably an exceptional case among the transition elements due to the half-filled d band and geometric frustrations in the fcc structure.

In conclusion, our ARPES data for the γ phase of manganese and their theoretical analysis by means of LDA + DMFT, an approach that accounts not only for band-structure effects on the LDA level but also allows for a full description of local effects of strong Coulomb correlations, provide evidence for the formation of Hubbard bands in metallic manganese. This is a qualitatively new aspect in the physics of transition metals.

REFERENCES

1. J. Hubbard, Proc. R. Soc. London, Ser. A **281**, 401 (1964).
2. A. Georges, G. Kotliar, W. Krauth, and M. J. Rozenberg, Rev. Mod. Phys. **68**, 13 (1996).
3. N. F. Mott, *Metal–Insulator Transitions* (Taylor and Francis, London, 1974; Nauka, Moscow, 1979).
4. A. I. Lichtenstein, M. I. Katsnelson, and G. Kotliar, Phys. Rev. Lett. **87**, 67 205 (2001).
5. P. Thiry *et al.*, Phys. Rev. Lett. **43**, 82 (1979).
6. J. A. Knapp, F. J. Himpsel, and D. E. Eastman, Phys. Rev. B **9**, 4952 (1979).
7. S. Hüfner and G. K. Wertheim, Phys. Lett. A **51**, 299 (1975).
8. C. Guillot *et al.*, Phys. Rev. Lett. **39**, 1632 (1977).
9. M. I. Katsnelson and A. I. Lichtenstein, J. Phys.: Condens. Matter **11**, 1037 (1999).
10. F. J. Himpsel, P. Heimann, and D. E. Eastman, J. Appl. Phys. **52**, 1658 (1981).
11. N. E. Zein, Phys. Rev. B **52**, 11 813 (1995).
12. V. L. Moruzzi, P. M. Marcus, and J. Kubler, Phys. Rev. B **39**, 6957 (1989).
13. A. F. Guillermet and G. Grimvall, Phys. Rev. B **40**, 1521 (1989).
14. B. Schirmer *et al.*, Phys. Rev. B **60**, 5895 (1999).
15. S. D. Kevan, *Angle-Resolved Photoemission: Theory and Current Applications* (Elsevier, Amsterdam, 1992), Stud. Surf. Sci. Catal., Vol. 74.
16. O. Rader and W. Gudat, in *Landolt–Börnstein*, New Series, Group III, Ed. by A. Goldmann (Springer, Berlin, 1999), Vol. 23 (C2).
17. D. J. Crockford, D. M. Bird, and M. W. Long, J. Phys.: Condens. Matter **3**, 8665 (1991).
18. A. Georges and G. Kotliar, Phys. Rev. B **45**, 6479 (1992).
19. V. I. Anisimov *et al.*, J. Phys.: Condens. Matter **9**, 7359 (1997).
20. A. I. Lichtenstein and M. I. Katsnelson, Phys. Rev. B **57**, 6884 (1998).
21. J. E. Hirsch and R. M. Fye, Phys. Rev. Lett. **56**, 2521 (1986).
22. O. K. Andersen, Phys. Rev. B **12**, 3060 (1975).
23. M. Jarrell and J. E. Gubernatis, Phys. Rep. **269**, 133 (1996).
24. W. Speier *et al.,* Phys. Rev. B **30**, 6921 (1984).
25. R. S. Fishman and S. H. Liu, Phys. Rev. B **59**, 8681 (1999).